



## City Research Online

### City, University of London Institutional Repository

---

**Citation:** Gkoktsi, K. & Giaralis, A. (2019). A multi-sensor sub-Nyquist power spectrum blind sampling approach for low-power wireless sensors in operational modal analysis applications. *Mechanical Systems and Signal Processing*, 116, pp. 879-899. doi: 10.1016/j.ymssp.2018.06.049

This is the accepted version of the paper.

This version of the publication may differ from the final published version.

---

**Permanent repository link:** <https://openaccess.city.ac.uk/id/eprint/19969/>

**Link to published version:** <https://doi.org/10.1016/j.ymssp.2018.06.049>

**Copyright:** City Research Online aims to make research outputs of City, University of London available to a wider audience. Copyright and Moral Rights remain with the author(s) and/or copyright holders. URLs from City Research Online may be freely distributed and linked to.

**Reuse:** Copies of full items can be used for personal research or study, educational, or not-for-profit purposes without prior permission or charge. Provided that the authors, title and full bibliographic details are credited, a hyperlink and/or URL is given for the original metadata page and the content is not changed in any way.

---

City Research Online:

<http://openaccess.city.ac.uk/>

[publications@city.ac.uk](mailto:publications@city.ac.uk)

---

# A multi-sensor sub-Nyquist power spectrum blind sampling approach for low-power wireless sensors in operational modal analysis applications

Kyriaki Gkoktsi<sup>a</sup> and Agathoklis Giaralis<sup>b\*</sup>

<sup>a</sup> AKT-II LTD, London, UK; [Kyriaki.Gkoktsi.1@akt-uk.co.uk](mailto:Kyriaki.Gkoktsi.1@akt-uk.co.uk)

<sup>b</sup> City, University of London, London, UK; [Agathoklis.Giaralis.1@city.ac.uk](mailto:Agathoklis.Giaralis.1@city.ac.uk)

## ABSTRACT

A novel multi-sensor power spectrum blind sampling (PSBS) approach is proposed supporting low-power wireless sensor networks (WSN) for Operational Modal Analysis (OMA) applications. The developed approach relies on arrays of wireless sensors, employing deterministic non-uniform in time multi-coset sampling to acquire structural response acceleration signals at sub-Nyquist sampling rates, treated as realizations of stationary random processes without making any assumption about the average signal frequency content and spectral support. The acquired compressed measurements are transmitted to a central server and collectively processed via a PSBS technique, herein extended to the multi-sensor case, to estimate the power spectral density matrix of an underlying spatially correlated stationary response acceleration random process directly from the compressed measurements. Structural modal properties are then extracted through standard frequency domain decomposition (FDD). The efficacy of the proposed approach to resolve closely-spaced modes is numerically tested for various data compression levels using noisy response acceleration signals of a white-noise excited finite element model of a space truss as well as field-recorded acceleration time-histories of an instrumented bridge under operational loading. It is shown that accurate mode shapes based on the modal assurance criterion can be obtained from as low as 89% less measurements compared to conventional non-compressive FDD at Nyquist sampling rate. Further, significant gains in energy consumption and battery lifetime prolongation of the order of years are estimated, assuming wireless sensors operating on multi-coset sampling at different data compression levels. It is, therefore, concluded that the proposed PSBS approach could provide long-term structural health monitoring systems with low-maintenance cost once wireless sensors with multi-coset sampling capabilities become commercially available.

**Keywords:** power spectral estimation; multi-coset sampling; sub-Nyquist sampling; operational modal analysis; wireless sensors; modal properties.

## 1. Introduction

Operational modal analysis (OMA) is a widely-used vibration-based approach for condition assessment, design verification, and health monitoring of civil engineering structures ([1],[2]). It derives dynamic structural properties (e.g. natural frequencies, mode shapes, and modal damping ratios) by acquiring and processing response acceleration signals from structures vibrating under low-amplitude ambient loads (e.g., due to wind or traffic). Excitation loads are not measured but assumed to attain a sufficiently flat spectrum within a relatively wide frequency range such that they are modelled as band-limited white noise capable of exciting the first few dominant modes of vibration.

The consideration of wireless sensor networks (WSNs) attracted the attention of the research community in the past 15 years to facilitate long-term OMA applications ([3]-[6]). Compared to arrays of wired sensors, WSNs allow for less obtrusive, more economical and rapid implementation of OMA, especially in monitoring large scale and geometrically complex civil engineering structures. In a typical WSN deployment for OMA (top panel in Fig. 1), sensors are equipped with analog-to-digital converters (ADCs) sampling uniformly in time structural response signals at rates higher than an assumed (target) Nyquist rate/frequency followed by appropriate low-pass filtering to eliminate aliasing and to increase resolution. The acquired measurements are stored at the sensor and *locally processed* by on-board micro-processors that typically perform off-line lossy or lossless data compression [7]-[9]. The main goal of this operation is the reduction of the data transmission payload within WSNs, which are constrained by the limited available wireless transmission bandwidth. It also aims to minimize the energy consumption at sensors and, therefore, the requirements for local energy harvesting and/or battery replacement, since wireless data transmission is by far the most power consuming operation in WSNs [3]. The encoded measurements (i.e., compressed data) are then wirelessly transmitted to a base station (server) where they are de-compressed to retrieve the originally acquired signals, or an estimate of them in case of lossy compression schemes. The latter can be further processed by standard OMA algorithms to derive structural dynamic properties. Despite these efforts, the power resources of current wireless sensors are limited by various factors such as the sampling frequency, the duration of each monitoring interval, the computational complexity of the on-board algorithms to be executed, the achieved data compression level, etc. [3],[4].

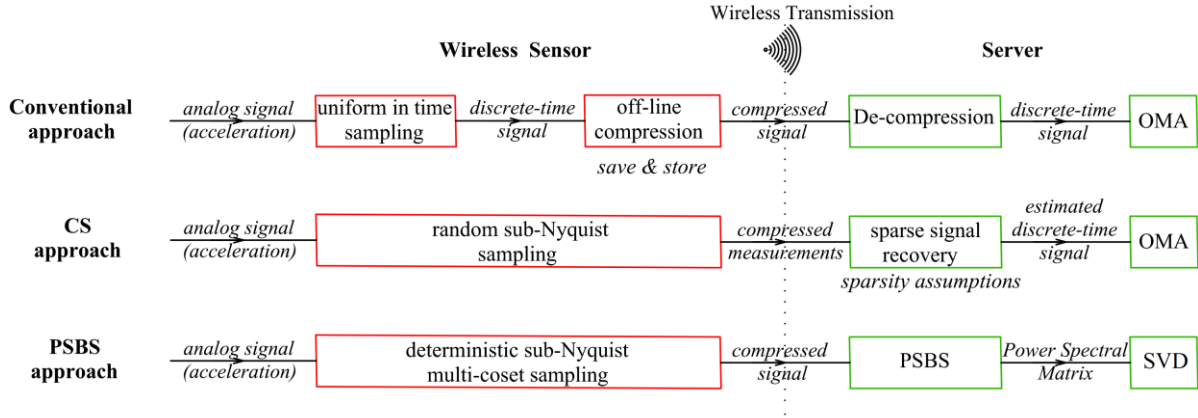


**Fig. 1.** Typical operations undertaken in a typical (top), a CS-based (middle), and a PSBS-based (bottom) WSN

To this end, it has been recently recognized that the compressive sensing (CS) paradigm involving simultaneous signal acquisition and compression at the sensor front-end can reduce energy consumption in wireless sensors [7] by minimizing the dimensions of the acquired measurements and, therefore, requirements for on-sensor data storage and local on-board data processing before wireless transmission (middle panel of Fig. 1). Specifically, in typical CS-based signal acquisition and processing approaches, signals are assumed to attain some level of “sparsity” on some basis (e.g. the Fourier basis), that is, to have a relatively small number of coefficients with non-negligible values once projected on a given basis which renders them “compressible” [10],[11]. Depending on the signal compressibility/sparsity level a sufficient number of measurements is acquired randomly in time at average sampling rates below Nyquist (i.e., sub-Nyquist rates). The compressed measurements are transmitted to the base station and post-processed by sparse signal recovery algorithms, involving the solution of an underdetermined system of linear equations [12], to obtain estimates of the significant signal coefficients on the assumed sparsifying basis.

O’Connor et al. [13],[14] successfully implemented the above standard CS-based approach in a long-term OMA field application in Michigan and reported appreciable gains in sensor energy consumption due to reduced data transmission rates compared to conventional Nyquist sampling. Mode shapes and natural frequencies of the monitored bridge were extracted using the standard peak-picking frequency domain decomposition (FDD) algorithm for OMA [2]. The latter step involved taking the singular value decomposition (SVD) of the power spectral density (PSD) matrix estimated from CS-based acquired and recovered response acceleration signals. Yang and Nagarajaiah [15] proposed an alternative CS-based approach for OMA in which mode shapes are extracted from modal structural responses obtained by application of blind source separation directly to randomly acquired CS measurements of structural response signals. Sparse signal recovery in the time-domain

was next applied to each compressed modal response vector to retrieve structural natural frequencies and modal damping ratios. Further, Yang *et al.* [16] demonstrated that blind source separation analysis may also be used in conjunction with uniform in time sampled measurements at sub-Nyquist rates (i.e., with possible aliasing) to extract modal properties of free vibrating structures from response acceleration signals as well as from video signals. Moreover, Park *et al* [17] derived analytically bounds on the required number of randomly acquired CS measurements to achieve accurate mode shape estimation from free vibration response of undamped multi-degree-of-freedom structures with known number of degrees of freedom; that is from multi-tone signals with known number of harmonics. In the latter work mode shapes are obtained by application of the SVD directly to CS measurements without taking any signal sparse recovery step.

Recognizing that the key for quality OMA in the context of the standard CS paradigm is the faithfulness of the recovered response acceleration signals from random measurements, Klis and Chatzi [18],[19] adopted a reweighted basis pursuit denoising problem formulation enabling enhanced accuracy in sparse signal recovery by relying on *a priori* knowledge of signal support in the frequency domain (i.e., spectral support) and noise level. In [18] such knowledge is gained by considering a small network of judiciously located wired sensors sampling in the conventional manner (i.e., uniformly-in-time at the Nyquist rate or above) and operating concurrently with an extensive CS-based WSN. The anticipated spectral support and noise level of signals acquired by the WSN is estimated by Fourier transforming the conventionally sampled signals at the server. This information is wirelessly communicated to the CS-based sensors to inform the rate of the random sampling and stored at the server for sparse recovery of enhanced accuracy. In [19], signal spectral support and noise level information is gained and updated in real-time by the wireless sensors which sample at uniform (Nyquist or above) rate and locally post-process Nyquist measurements. This information is communicated to the server which sends back to the sensors “optimal” specifications for random CS-based sampling. Finally, sensors transmit compressed measurements to the server where signal recovery in time-domain is accomplished as well as OMA using standard approaches. This so-called spectral-temporal compressive sensing (STCS) approach is shown to be more accurate for mode shape estimation compared to conventional CS-based approaches at the expense of an involved two-way data communication protocol between the WSN and the server.

Herein, a novel approach for frequency domain OMA is put forth supporting low-complexity and low-energy consumption WSNs by acquiring and compressing response acceleration measurements at the front-end of sensors, similar to the standard CS-based approach taken in [13],[14], but without necessitating any *prior* knowledge of signal spectral support or noise level as required in [18],[19] (see bottom panel in Fig. 1). Specifically, the proposed approach treats

response acceleration signals from arrays of sensors as realizations of a spatially correlated temporal stationary random process. The approach estimates second-order statistics of this process (i.e., the PSD matrix) by application of power spectrum blind sampling (PSBS) to compressed measurements acquired by all sensors in the network using a particular deterministic periodic non-uniform-in-time sampling scheme known as multi-coset sampling [20]-[26]. To this aim, compressed samples acquired by each sensor are centrally transmitted to a server where PSD matrix estimation is undertaken. Next, structural modal properties can be extracted by taking the SVD of the PSD matrix estimate in the context of frequency domain-based OMA [2]. Note that PSBS was originally developed for cognitive radio applications aiming to sample/sense the PSD of weak sub-Nyquist sampled noise-corrupted telecommunication signals and to efficiently detect unoccupied bands in a wide spectral range [21]-[23]. To this effect, PSBS has been previously considered to estimate the PSD of stationary random processes/signals of different frequency content by treating multi-coset samples from a single sensor without any prior knowledge of signal spectral support, therefore the term “blind” (see e.g., [20]-[23]). In this regard, this work makes a theoretical contribution by extending PSBS to the multi-sensor case to estimate all elements of the full PSD matrix of an underlying stationary spatially-correlated random process. To this end, this paper presents the underpinning mathematical background of PSBS with multi-coset sampling and discusses practical consequences of various assumptions made in the theoretical development. Further, in the numerical part of the paper, the accuracy of the proposed approach is assessed against mode shapes and natural frequencies extracted using the peak-picking FDD in conjunction with PSD matrices estimated through standard spectral estimation techniques applicable to Nyquist sampled data. The aim is to quantify the level of data compression and consequent battery life in wireless sensor nodes made possible through multi-coset sampling without compromising the accuracy of the extracted mode shapes and natural frequencies compared to Nyquist sampled data. For comparative numerical assessment between multi-coset PSBS approach and the standard CS-based paradigm for OMA implemented by O'Connor et al. [13],[14] as well as the STCS approach pioneered by Klis and Chatzi [18],[19], the interested reader is directed to references [27] and [28], respectively.

In the remainder of the paper, Section 2 reviews the details of the multi-coset sampling and discusses recent relevant advances in hardware implementation supporting the practical merit of this work since sensors with multi-coset sampling capabilities are not currently commercially available. Section 3 presents the theoretical background underpinning the proposed multi-sensor PSBS-based approach for OMA, while Section 4 discusses the design of optimal multi-coset sampling schemes based on a number of simplified assumptions which promote a spectral agnostic attribute of the proposed approach. In Sections 5 and 6 the accuracy of the herein developed approach is

numerically assessed against standard non-compressive FDD-based OMA by considering computer-simulated noisy acceleration response signals pertaining to a white-noise excited space truss with two closely-spaced modes and field-recorded acceleration data taken from a monitored bridge located in Switzerland, respectively. Further, Section 7 quantifies gains in energy consumption and battery lifetime achieved by the PSBS-based approach by adopting specifications of a certain conventional wireless sensor, while Section 8 summarizes concluding remarks.

## 2. Multi-coset sampling

Let  $x(t)$  be a continuous in time  $t$  real-valued wide-sense-stationary random signal (or stochastic process) characterized in the frequency domain by a power spectrum band-limited to  $2\pi/T$ . Consider, further, the grid of Nyquist samples  $x[v]=x(vT)$ , where  $v \in \mathbb{Z}_+$ , of the random signal (or of a realization of the stochastic process). Multi-coset sampling involves partitioning the Nyquist grid in  $K$  blocks of  $N$  consecutive samples and acquiring only  $M (<N)$  samples from each block [22],[25]. The location of the  $M$  samples within each  $N$ -length block is defined by the sampling pattern sequence

$$\mathbf{s} = [s_0, s_1, \dots, s_{M-1}], \quad (1)$$

applicable to all  $K$  blocks. The elements of the above sequence are non-negative integers sorted in ascending order without repetition (i.e.,  $s_i \neq s_j, \forall i \neq j$ ). They define the difference set

$$\Omega = \{|s_i - s_j|, s_i, s_j \in \mathbf{s}\}, \quad (2)$$

arising naturally in the computation of correlation functions of discrete-time signals considered in the following section for the purpose of spectral estimation.

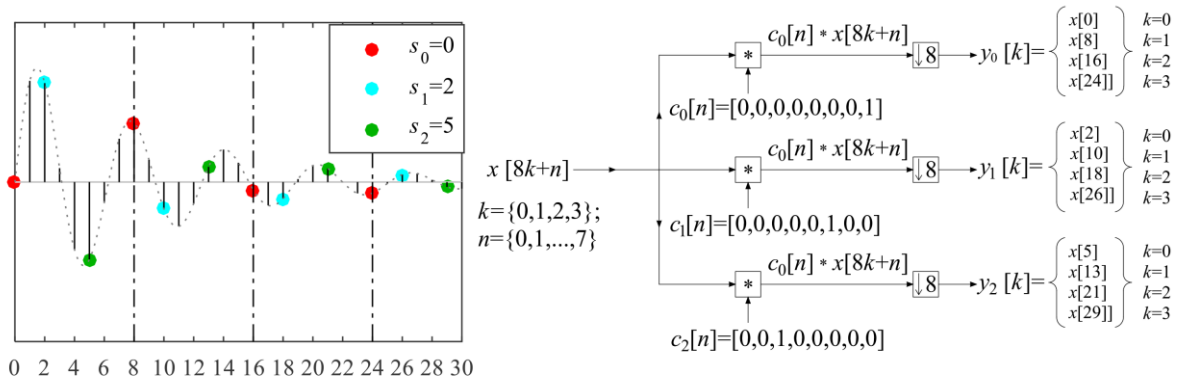


**Fig. 2.** Example of multi-coset sampling applied to a 32-long Nyquist sampled discrete-time signal with  $M=3, N=8, K=4$ , and sampling pattern  $\mathbf{s}=[0, 2, 5]$ .

For illustration, the left panel of Fig. 2 applies multi-coset sampling with pattern  $\mathbf{s}=[0, 2, 5]$  to a 32-long signal  $x[v]$ ,  $v=\{0,1,\dots,31\}$ , partitioned in  $K=4$  blocks of length  $N=8$ . The

adopted sampling pattern acquires  $M=3$  samples (“cosets”) from each block whose location is defined by the elements  $s_i, i=\{0,1,2\}$  of the pattern as shown with colored circular markers in Fig. 2. This particular pattern picks the first, the third, and the sixth Nyquist sample from each block.

Evidently, multi-coset sampling is *periodic* with period  $N$ ; *non-uniform in time* since any subset of  $M$  samples may be selected from the  $N$  Nyquist samples in the block; and *deterministic* since the position of the  $M$  samples on the Nyquist grid is *a priori* fixed through the sampling sequence. From a signal acquisition viewpoint, multi-coset sampling can be implemented by utilizing  $M$  interleaved channels of ADC units, operating at a sampling rate  $1/(NT)$ , (i.e.,  $N$  times slower than the Nyquist rate  $1/T$ ) [22]. At the  $i$ -th ( $i=\{0, 1, \dots, M-1\}$ ) channel, the discrete-time signal  $x[v]$  is shifted by  $s_i$  samples and then uniformly sampled at  $1/(NT)$  rate. In this respect, an overall average sampling rate of  $M/(NT)$  is attained accounting for all  $M$  channels. Therefore, the ratio  $M/N$  defines the signal compression achieved by multi-coset sampling and is hereafter termed *compression ratio (CR)*. This ratio takes on values within the range  $0 \leq CR=M/N \leq 100\%$ : smaller  $CR$  values imply higher signal compression, while the limiting case of  $CR=100\%$  (i.e.,  $M=N$ ) corresponds to conventional uniform in time sampling at Nyquist rate. In this context, the  $K$  compressed (sub-Nyquist) samples acquired at the  $i$ -th channel,  $y_i$ , can be mathematically written through the filtering operation

$$y_i[k] = \sum_{n=0}^{1-N} c_i[-n] x[kN+n] = \sum_{n=1-N}^0 c_i[n] x[kN-n], \quad k=0,1,\dots,K-1, \quad (3)$$

where the filter coefficients are given as

$$c_i[n] = \begin{cases} 1, & n = s_i, \\ 0, & n \neq s_i, \end{cases} \quad (4)$$

in which  $n=[1-N, 2-N, \dots, 0]$  is arranged in descending order. The use of the last two equations is exemplified in the right panel of Fig. 2 showing a block diagram of an ideal multi-coset sampler implementing the previously discussed sampling example depicted in the left panel of Fig. 2. It comprises  $M=3$  channels and at the  $i$ -th channel, ( $i=\{0,1,2\}$ ) the 32-long discrete-time signal  $x[v]$  written as  $x[kN+n]$ , with  $N=8$ ,  $K=4$ ,  $k=\{0,1,2,K-1\}$  and  $n=\{0,1,\dots,N-1\}$ , is convolved with the filter coefficient sequences  $c_i[n]$  shown in Fig. 2 and down-sampled by  $N=8$  to generate the output/compressed measurements  $y_i$ . Note that overall only 12 measurements are acquired from a total of 32 available Nyquist samples corresponding to  $CR=12/32=37.5\%$  which further coincides with  $M/N=3/8$ .

Notably, recent developments in hardware architecture paved the way for the design of multi-coset sensor prototypes using banks of time-interleaved ADC units (channels) [29]. Specifically, a discrete-time version of a multi-coset sampler was proposed in [22] to acquire compressed

measurements from a wideband non-sparse signal based on the modulated wideband converter prototype developed by Mishali and Eldar [30]. Further, a dual-rate hardware architecture was designed by Moon et al. [31], comprising a pair of time-interleaved under-sampling ADCs that accommodate two different sampling patterns with a small frequency offset to iteratively acquire delayed versions of the same input signal at sub-Nyquist sampling rates. More recently, Jingchao et al. [32] designed a prototype multi-coset sampler that can support up to 10 interleaved sub-Nyquist ADC sampling channels, being also capable to rectify any potential error due to channel diversity gain and/or time synchronization among the various ADC channels. In view of the above developments, the remainder of this paper assumes the availability of wireless sensor nodes incorporating ideal multi-coset samplers even though such sensors are not commercially available yet.

### 3. Proposed multi-sensor power spectrum blind sampling (PSBS) for OMA

Consider a network of  $D$  identical wireless sensor nodes with multi-coset samplers of  $M$  channels each, operating on the same sampling pattern across their channels. The considered WSN is assumed to be placed along a structure, measuring  $D$  acceleration responses under ambient excitation. Let  $x^a[v], x^b[v]$  with  $a, b = 1, 2, \dots, D$  be the unknown discrete-time signals, sampled at Nyquist rate from the band-limited continuous-time acceleration response random signals (i.e., stochastic processes)  $x^a(t)$  and  $x^b(t)$  respectively. The first step of the herein proposed multi-sensor PSBS approach is the recovery of the cross-correlations

$$r_{x^a x^b}[\ell] = E_x \{ x^a[v] x^b[v - \ell] \}, \ell \in \mathbb{Z}, \quad (5)$$

computed among all input acceleration signals  $x^a[v], x^b[v]$  to the  $a, b = \{1, 2, \dots, D\}$  devices. In the last equation and hereafter  $E_a \{ \cdot \}$  is the mathematical expectation operator with respect to  $a$ . As illustrated in Fig. 3, the above step can be achieved through the acquisition and central (collective) processing of  $M \times D$  output/compressed sequences  $y_i^a[k], y_j^b[k]$  from all  $i, j = \{0, 1, \dots, M-1\}$  channels of the  $a, b = \{1, 2, \dots, D\}$  devices, using the multi-coset sampling strategy detailed in the previous sub-section. The mathematical details involved are presented in the following sub-section.

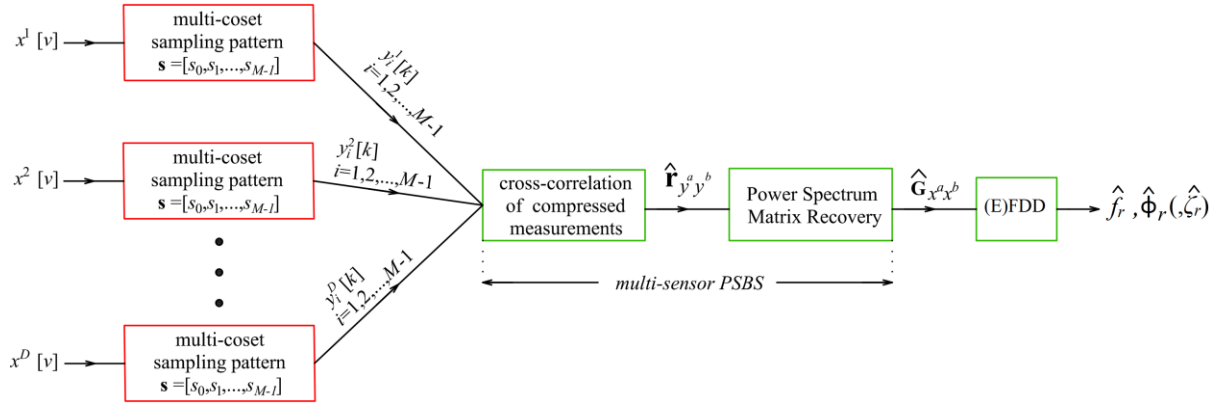


**Fig. 3.** Workflow of the multi-sensor PSBS approach for OMA

### 3.1. Cross-correlation estimation of sub-Nyquist measurements

Consider the cross-correlation sequences of the compressed measurements

$$r_{y_i^a, y_j^b}[\ell] = E_y \{ y_i^a[k] y_j^b[k - \ell] \}, \quad (6)$$

which are collected in the cross-correlation matrix  $\mathbf{r}_{y^a y^b} \in \mathbb{R}^{M^2 \times D}$  written as

$$\mathbf{r}_{y^a y^b}[\ell] = \begin{bmatrix} r_{y_0^a, y_0^b}[\ell] \cdots r_{y_0^a, y_{(M-1)}^b}[\ell] & r_{y_1^a, y_0^b}[\ell] \cdots r_{y_{(M-1)}^a, y_{(M-1)}^b}[\ell] \end{bmatrix}^T, \quad (7)$$

where the superscript ‘‘T’’ denotes matrix transposition. Similarly, consider the following cross-correlation matrix  $\mathbf{r}_{x^a x^b} \in \mathbb{R}^{N \times D}$

$$\mathbf{r}_{x^a x^b}[\ell] = \begin{bmatrix} r_{x^a x^b}[\ell N] & r_{x^a x^b}[\ell N + 1] \cdots r_{x^a x^b}[(\ell + 1)N - 1] \end{bmatrix}^T, \quad (8)$$

collecting the cross-correlation sequences of the response acceleration signals in Eq.(5).

It can be shown that the above two cross-correlation matrices are related through the expression

$$\mathbf{r}_{y^a y^b}[\ell] = \sum_{p=0}^1 \mathbf{R}_c[p] \mathbf{r}_{x^a x^b}[\ell - p], \quad (9)$$

by means of the sampling pattern cross-correlation matrix  $\mathbf{R}_c \in \mathbb{R}^{M^2 \times N}$  given by

$$\mathbf{R}_c[p] = \begin{bmatrix} \mathbf{r}_{c_0, c_0}[p] \cdots \mathbf{r}_{c_0, c_{M-1}}[p] & \mathbf{r}_{c_1, c_0}[p] \cdots \mathbf{r}_{c_{M-1}, c_{M-1}}[p] \end{bmatrix}^T, \quad p \in \mathbb{Z}. \quad (10)$$

The latter matrix is populated with the pattern cross-correlation sequences in Eq. (4), expressed as

$$r_{c_i, c_j}[p] = \sum_{n=1-N}^0 c_i[n] c_j[n - p] = \delta[p - (s_i - s_j)], \quad (11)$$

where  $\delta[\cdot]$  is the Dirac delta function. Notably, the elements of the pattern cross-correlation matrix relating the matrices in Eqs. (7) and (8) depends only on the adopted sampling pattern sequence in Eq. (1) through the difference set  $\Omega$  defined in Eq. (2).

Assume further that the cross-correlation sequences  $\mathbf{r}_{x^a x^b}[\ell]$  in Eq. (8) take on negligible values outside a range  $-L \leq \ell \leq L$ . Then, the relationship in Eq. (9) can be cast in matrix form

$$\mathbf{r}_{y^a y^b} = \mathbf{R}_c \mathbf{r}_{x^a x^b}, \quad (12)$$

where the “output” correlation matrix  $\mathbf{r}_{y^a y^b} \in \mathbb{R}^{M^2(2L+1) \times D}$  corresponding to the compressed measurements is given as

$$\mathbf{r}_{y^a y^b} = \begin{bmatrix} \mathbf{r}_{y^a y^b}^T [0] \cdots \mathbf{r}_{y^a y^b}^T [L] & \mathbf{r}_{y^a y^b}^T [-L] \cdots \mathbf{r}_{y^a y^b}^T [-1] \end{bmatrix}^T, \quad (13)$$

and the “input” correlation matrix  $\mathbf{r}_{x^a x^b} \in \mathbb{R}^{N(2L+1) \times D}$  corresponding to the structural response acceleration signals is given as

$$\mathbf{r}_{x^a x^b} = \begin{bmatrix} \mathbf{r}_{x^a x^b}^T [0] \cdots \mathbf{r}_{x^a x^b}^T [L] & \mathbf{r}_{x^a x^b}^T [-L] \cdots \mathbf{r}_{x^a x^b}^T [-1] \end{bmatrix}^T. \quad (14)$$

In this setting, the pattern matrix  $\mathbf{R}_c \in \mathbb{R}^{M^2(2L+1) \times N(2L+1)}$  attains a sparse structure as in

$$\mathbf{R}_c = \begin{bmatrix} \mathbf{R}_c[0] & \mathbf{O} & \cdots & \mathbf{O} & \mathbf{R}_c[1] \\ \mathbf{R}_c[1] & \mathbf{R}_c[0] & \mathbf{O} & \ddots & \mathbf{O} \\ \mathbf{O} & \mathbf{R}_c[1] & \mathbf{R}_c[0] & \ddots & \vdots \\ \vdots & \ddots & \ddots & \ddots & \mathbf{O} \\ \mathbf{O} & \cdots & \mathbf{O} & \mathbf{R}_c[1] & \mathbf{R}_c[0] \end{bmatrix}, \quad (15)$$

with  $\mathbf{O}$  being the zero matrix. Note that Eq. (12) defines an overdetermined system of linear equations which can be solved for  $\mathbf{r}_{y^a y^b}$  provided that  $\mathbf{R}_c$  is full column rank. The latter condition requires that  $M^2 \geq N$  which can be readily satisfied in specifying the multi-coset sampling scheme. For example, the illustrative sampling scheme in Fig. 2 satisfies the above requirement as  $M^2=9 > N=8$ . Importantly, the solution of Eq. (12) for  $\mathbf{r}_{y^a y^b}$  does not necessitate making any restrictive assumption on the frequency content of the underlying stationary stochastic process. In this regard, the herein developed approach is equally applicable to narrow-band (e.g., single-tone), multi-band (e.g., multi-tone), and wide-band (e.g., band-limited white-noise) stationary signals.

To support practical numerical implementation, consider next the unbiased estimator of the output cross-correlation function  $r_{y_i^a y_j^b}[\ell]$  in Eq. (6) defined by

$$\hat{r}_{y_i^a y_j^b}[\ell] = \frac{1}{K - |\ell|} \sum_{k=\max\{0, \ell\}}^{K-1+\min\{0, \ell\}} y_i^a[k] y_j^b[k - \ell], \quad \ell = \{-L, \dots, 0, \dots, L\}, \quad (16)$$

and the estimated output cross-correlation matrix  $\hat{\mathbf{r}}_{y^a y^b} \in \mathbb{R}^{M^2(2L+1) \times D}$  constructed in the same manner as the matrix in Eq.(13). The following weighted least square minimization criterion is herein adopted

to solve (“invert”) numerically Eq.(12)

$$\begin{aligned}
 \hat{\mathbf{r}}_{x^a x^b} &= \underset{\mathbf{r}_{x^a x^b}}{\operatorname{argmin}} \left\| \hat{\mathbf{r}}_{y^a y^b} - \mathbf{r}_{y^a y^b} \right\|_{\mathbf{W}}^2 \\
 &= \underset{\mathbf{r}_{x^a x^b}}{\operatorname{argmin}} \left\| \hat{\mathbf{r}}_{y^a y^b} - \mathbf{R}_c \mathbf{r}_{x^a x^b} \right\|_{\mathbf{W}}^2, \\
 &= \underset{\mathbf{r}_{x^a x^b}}{\operatorname{argmin}} \left( \hat{\mathbf{r}}_{y^a y^b} - \mathbf{R}_c \mathbf{r}_{x^a x^b} \right)^\top \mathbf{W} \left( \hat{\mathbf{r}}_{y^a y^b} - \mathbf{R}_c \mathbf{r}_{x^a x^b} \right)
 \end{aligned} \tag{17}$$

where  $\|\mathbf{a}\|_{\mathbf{W}}^2 = \mathbf{a}^\top \mathbf{W} \mathbf{a}$  is the weighted version of the Euclidean norm, with  $\mathbf{W} \in \mathbb{R}^{M^2(2L+1) \times M^2(2L+1)}$  being a positive-definite weighting matrix. The latter matrix can be defined independently of  $\mathbf{r}_{x^a x^b}$  and, in fact, can be arbitrarily chosen. For instance, in the trivial case of adopting equal unit weights,  $\mathbf{W}$  is set equal to the unitary matrix yielding a least-square minimization criterion in Eq. (17). Nevertheless, in Section 4, an approach for weighting matrix specification is reviewed based on a criterion supporting spectral estimation irrespective of the frequency content of the stationary signals acquired.

In this setting, the objective function of the minimization problem in Eq. (17) is

$$f_{WLS}(\mathbf{r}_{x^a x^b}) = \left( \hat{\mathbf{r}}_{y^a y^b} - \mathbf{R}_c \mathbf{r}_{x^a x^b} \right)^\top \mathbf{W} \left( \hat{\mathbf{r}}_{y^a y^b} - \mathbf{R}_c \mathbf{r}_{x^a x^b} \right), \tag{18}$$

which is convex, attaining a minimum at

$$\hat{\mathbf{r}}_{x^a x^b} = \left( \mathbf{R}_c^\top \mathbf{W} \mathbf{R}_c \right)^{-1} \mathbf{R}_c^\top \mathbf{W} \hat{\mathbf{r}}_{y^a y^b}, \tag{19}$$

under the condition  $\frac{\partial f_{WLS}(\mathbf{r}_{x^a x^b})}{\partial \mathbf{r}_{x^a x^b}} = \mathbf{0}$ , where the superscript “-1” denotes matrix inversion. To this

end, given a multi-coset sampling pattern and a weighting matrix  $\mathbf{W}$ , Eq. (19) can be readily used to compute the cross-correlation matrix of the response acceleration signals from the cross-correlation estimates of the sub-Nyquist measurements acquired by the  $D$  multi-coset samplers. This can be achieved in a computationally economical manner even for relatively large values of  $L$  (depending on the desired resolution in the frequency domain as is explained in the following sub-section), since the sparse structure of  $\mathbf{R}_c \in \mathbb{R}^{M^2(2L+1) \times N(2L+1)}$  shown in Eq.(15) facilitates efficient matrix inversion.

Following the block diagram in Fig. 3, the remainder of this section delineates the steps of using the matrix  $\hat{\mathbf{r}}_{x^a x^b}$  to estimate the PSD matrix of response acceleration signals and extracting modal structural properties. Section 4 discusses an approach for optimal design of the sampling pattern and the weighting matrix that minimizes the spectral estimation error in the mean sense.

### 3.2. Power Spectral Matrix Recovery

Let  $P_{x^a x^b}(\omega)$  be the cross-PSD of  $x^a[v]$  and  $x^b[v]$  given through the discrete-time Fourier transform as

$$P_{x^a x^b}(\omega) = \sum_{p=-\infty}^{\infty} r_{x^a x^b}[p] e^{-ip\omega}, \quad 0 \leq \omega \leq 2\pi \quad (20)$$

where  $i = \sqrt{-1}$ . This PSD is further discretized in the frequency domain and cast in matrix form

$$\mathbf{G}_{x^a x^b} = \mathbf{F}_{(2L+1)N} \mathbf{r}_{x^a x^b}, \quad (21)$$

where  $\mathbf{F}_{(2L+1)N} \in \mathbb{C}^{N(2L+1) \times N(2L+1)}$  is the standard discrete Fourier transform (DFT) matrix and  $\mathbf{G}_{x^a x^b} \in \mathbb{C}^{N(2L+1) \times D}$  is the PSD matrix computed at the uniform discrete set of frequencies  $\omega = [0, \Delta\omega, 2\Delta\omega, \dots, ((2L+1)N-1)\Delta\omega]$ , with step  $\Delta\omega = \frac{2\pi}{(2L+1)N}$ . The latter is an important application-dependent quantity

as it governs the frequency resolution of the sought PSD matrix and, ultimately, the accuracy of modal properties. Notably, for a fixed value of  $N$  (pre-specified by the adopted multi-coset sampling scheme),  $\Delta\omega$  depends only on the parameter  $L$  which is associated with the support of the correlation sequences in Eqs. (13) and (14). Conveniently, *the value of  $L$  can be freely selected independently of the multi-coset sampling scheme* based on practical considerations related to the properties of the monitored structure. For instance, the monitoring of lightly-damped structures characterized by response acceleration PSD functions with sharp peaks requires adopting relatively large  $L$  values leading to sufficiently small  $\Delta\omega$  and, therefore, to enhanced frequency domain resolution achieving quality estimates of the natural frequencies. Further, the closer-spaced the natural frequencies are, the larger the adopted  $L$  should be to allow for resolving modes of vibration in the context of frequency domain-based OMA [2].

Making use of Eqs. (19) and (21), the following estimator of response accelerations PSD matrix is reached

$$\hat{\mathbf{G}}_{x^a x^b} = \mathbf{F}_{(2L+1)N} \hat{\mathbf{r}}_{x^a x^b} = \mathbf{F}_{(2L+1)N} \left( \mathbf{R}_c^T \mathbf{W} \mathbf{R}_c \right)^{-1} \mathbf{R}_c^T \mathbf{W} \hat{\mathbf{r}}_{y^a y^b}. \quad (22)$$

The latter expression provides a convenient formula to estimate the sought PSD matrix from the cross-correlation estimator applied directly to the sub-Nyquist/compressed acceleration measurements centrally collected from the WSN of  $D$  multi-coset samplers as shown diagrammatically in Fig. 3.

It is noted in passing that the herein developed multi-sensor PSBS approach differs significantly from the co-operative WSN for input signal spectral estimation investigated in [24] in both the nature of the problem addressed and the assumptions invoked. Drawing an analogy between the

present OMA problem and solution, and the telecommunications problem treated in [24], the latter would be interpreted in OMA terms as an approach for PSD estimation of the ambient excitation force with prior knowledge on the frequency response function (FRF) matrix of the vibrating structural system. On the contrary, the herein developed PSBS-based framework addresses output-only system identification within the OMA context under the assumption of linear vibrating structure excited by stationary excitation forces which are assumed to attain a sufficiently flat PSD. This aim is achieved by applying the SVD to the PSD matrix estimate in Eq.(22) following standard frequency domain-based OMA algorithms as briefly discussed in the following sub-section.

### *3.3. Frequency Domain Decomposition (FDD) for mode shape estimation*

The above developed multi-sensor PSBS approach for PSD matrix estimation can be fused with any qualified algorithm for frequency domain-based OMA [2] to extract structural modal properties. In the numerical part of this work, the standard peak-picking frequency domain decomposition (FDD) algorithm for OMA [2] is employed which relies on applying the SVD to the PSD matrix estimate  $\hat{\mathbf{G}}_{x^a x^b}$  in Eq. (22), i.e.,

$$\hat{\mathbf{G}}_{x^a x^b} = \mathbf{U}\mathbf{\Sigma}\mathbf{V}^T, \quad (23)$$

where  $\mathbf{\Sigma}$  is a diagonal positive semi-definite matrix comprising the singular values  $\Sigma_{rr}$ , and  $\mathbf{U}$ ,  $\mathbf{V}$  are the unitary singular matrices collecting the left and right singular vectors, respectively. Under the assumption of linearly vibrating structures, the singular values  $\Sigma_{rr}$  correspond to the PSDs of the uncorrelated modal coordinates and carry information of structural resonant (natural) frequencies,  $f_r$ ,  $r = \{1, 2, \dots, R\}$ , related to the  $R$  excited modes of vibration. Further, the left singular vector  $\mathbf{U}$  provides valid estimates of the mode shapes  $\hat{\phi}_r$ ,  $r = \{1, 2, \dots, R\}$ , related to the frequencies  $\hat{f}_r$  of the dominant singular values [2]. In case estimation of modal damping properties is desired, extended frequency domain decomposition (EFDD) algorithms may be applied [33],[34]. Such algorithms consider transforming the local (band-limited) PSDs associated with vibration modes identified by the singular value data in Eq.(23) to the time domain via inverse Fourier transform. The thus derived time domain data approximate correlation functions of SDOF systems whose properties can be extracted using any time-domain system identification technique to retrieve estimates of modal natural frequencies,  $\hat{f}_r$ , and modal damping ratios,  $\hat{\zeta}_r$ . Details on the mathematical background of the FDD algorithm and its extended variants allowing for modal damping estimation can be found in [2] and references therein.

#### 4. Design of the multi-coset sampling pattern

Common approaches for designing multi-coset sampling schemes supporting efficient correlation function estimation from sub-Nyquist measurements aim to define a difference set in Eq.(2) such that all possible differences are generated up to  $s_{M-1}$  using the shortest possible sampling pattern sequence in Eq. (1). This is achieved by relying on the concept of (minimum) sparse ruler (see e.g. [35] and references therein). Herein, a significantly different approach for designing the multi-coset sampling pattern is adopted based on a PSD error minimization criterion as originally considered in [26]. This consideration is motivated by the fact that the efficacy of the proposed PSBS approach for quality OMA relies on the accuracy of the PSD matrix estimate.

Specifically, the adopted optimal multi-coset sampling design approach assumes the case of a single sensor used to acquire a white noise random signal (process)  $x_w[v] = x_w(vT)$  bandlimited to  $2\pi/T$ . Apart from facilitating mathematical manipulations, this scenario preserves the general applicability of the sampling solution to the case of networks of identical sensors considered in the previous section while ensures the indifference of the method to the spectral content of the acquired stationary signals. In fact, white noise time-histories are least structured in time domain and least sparse in frequency domain and, in this regard, the case considered can be viewed as a worst-case scenario from the sub-Nyquist/compressed signal acquisition viewpoint. Before embarking on formulating the optimization problem for multi-coset sampling pattern design, it is first necessary to specify the weighting matrix  $\mathbf{W}$  appearing in Eq.(22). This problem is addressed in the following sub-section.

##### 4.1. Specification of the weighting matrix $\mathbf{W}$

As discussed in Section 3.2, a weighting matrix  $\mathbf{W}$  can be employed to improve the accuracy of the estimated cross-correlation matrix  $\hat{\mathbf{r}}_{x^a x^b}$  in Eq. (17) and, therefore, the accuracy of the PSD matrix in Eq.(22). To this aim the weighting matrix  $\mathbf{W}$  is specified in [26] such that it minimizes the mean square error (MSE)  $E_x \left\{ \left\| \hat{\mathbf{G}}_x - \mathbf{G}_x \right\|_2^2 \right\}$ , where  $\|\mathbf{a}\|_2^2$  is the standard Euclidean norm,  $\mathbf{G}_x \in \mathbb{R}^{N(2L+1) \times 1}$  is the PSD of the white noise process  $x_w$  discretized in frequency domain as discussed in Section 3.2, and  $\hat{\mathbf{G}}_x \in \mathbb{R}^{N(2L+1) \times 1}$  is the estimator of  $\mathbf{G}_x$  given by setting  $x^a[v] = x^b[v] = x_w[v]$  in Eq.(22). That is,

$$\mathbf{W}_{\text{MSE}} = \underset{\mathbf{W}}{\text{argmin}} E_x \left\{ \left\| \hat{\mathbf{G}}_x - \mathbf{G}_x \right\|_2^2 \right\}. \quad (24)$$

Clearly, the above criterion for defining the weighting matrix enhances the accuracy of the estimator in Eq.(22) applicable to the multi-sensor case with identical  $D$  sensors, while the white noise signal assumption does not jeopardize general applicability of the PSBS approach of Section 3

to any stationary signal: the approach is agnostic with respect to stationary signal frequency content and there is no particular reason to anticipate that improved performance is achieved by assuming signals with alternative frequency content in solving Eq.(24), with the stipulation that no prior knowledge of the response acceleration signals to be acquired is available. Conveniently, under the white noise signal assumption, the minimization problem in Eq.(24) is solved in closed form as [26]

$$\mathbf{W}_{\text{MSE}} = \frac{1}{\sigma_x^4} \cdot \begin{bmatrix} K \cdot \mathbf{I}_{M^2} & 0 & \cdots & 0 & 0 & \cdots & 0 \\ 0 & (K-1) \cdot \mathbf{I}_{M^2} & \cdots & 0 & 0 & \cdots & 0 \\ \vdots & \vdots & \ddots & \vdots & \vdots & \ddots & \vdots \\ 0 & 0 & \cdots & (K-L) \cdot \mathbf{I}_{M^2} & 0 & \cdots & 0 \\ 0 & 0 & \cdots & 0 & (K-L) \cdot \mathbf{I}_{M^2} & \cdots & 0 \\ \vdots & \vdots & \ddots & \vdots & \vdots & \ddots & \vdots \\ 0 & 0 & \cdots & 0 & 0 & \cdots & (K-1) \cdot \mathbf{I}_{M^2} \end{bmatrix}, \quad (25)$$

where  $\mathbf{I}_{M^2}$  is the unitary matrix of size  $M^2 \times M^2$ , and  $\sigma_x^2$  is the variance of the assumed white noise process  $x_w$ .

#### 4.2. Optimal multi-coset sampling pattern

Having established the block-diagonal weighting matrix in Eq.(25), the multi-coset pattern in Eq. (1) is derived such that the following objective function involving the normalized MSE  $E_x \left\{ \left\| \hat{\mathbf{G}}_x - \mathbf{G}_x \right\|_2^2 \right\}$  is minimized [26]

$$f_{\text{MSE}}(\mathbf{s}) = \frac{1}{\sigma_x^4 (2L+1)N} (K(2L+1) - L(L+1)) E_x \left\{ \left\| \hat{\mathbf{G}}_x - \mathbf{G}_x \right\|_2^2 \right\} = \sum_{n=1}^N \frac{1}{\alpha_n(\mathbf{s})}. \quad (26)$$

The term  $\alpha_n(\mathbf{s}) \in \mathbb{Z}^{1 \times 1}$  is a scalar computed for every  $n \in \{1, 2, \dots, N\}$  as

$$\alpha_n(\mathbf{s}) = \sum_{i=0}^{M-1} \sum_{j=0}^{M-1} \delta[-n+1-(s_i-s_j)] + \delta[N-n+1-(s_i-s_j)], \quad (27)$$

and  $\mathbf{s}$  is the sequence of  $M$  positive integers in Eq. (1). Therefore, the optimally designed multi-coset sampling pattern that minimizes the MSE  $E_x \left\{ \left\| \hat{\mathbf{G}}_x - \mathbf{G}_x \right\|_2^2 \right\}$  is determined by solving the problem [26]

$$\mathbf{s}_{\text{MSE}} = \arg \min_{\mathbf{s}} \sum_{n=1}^N \frac{1}{\alpha_n(\mathbf{s})}, \quad (28)$$

subject to the following constraints

$$\begin{aligned}
 \alpha_n(\mathbf{s}) &\geq 1, \quad \forall n \in \left\{ 2, 3, \dots, \left\lfloor \frac{1}{2}N \right\rfloor + 1 \right\}, \\
 s_0 &= 0, \\
 s_{M-1} &= \left\lfloor \frac{1}{2}N \right\rfloor, \\
 s_i &\in \left\{ s_{i-1} + 1, \dots, \left\lfloor \frac{1}{2}N \right\rfloor - M + i + 1 \right\}, \quad \forall i \in \{1, 2, \dots, M-2\},
 \end{aligned} \tag{29}$$

where  $\lfloor \cdot \rfloor$  is the mathematical floor operator. The solution of the above optimization problem is computationally demanding but needs to be solved only once as part of the design of the multi-coset sensor. It is herein solved via standard exhaustive pattern search. Further mathematical details on the design criterion of the adopted multi-coset sampling pattern and the weighted matrix can be found in [26]. For the purposes of this work, it suffices to recognize that for a given pair of  $(M, N)$  values and the associated  $CR = M/N$ , an optimal multi-coset pattern is derived by solving the problem in Eq.(28). This is used in the ensuing numerical work to obtain the compressed measurements in Eq.(3) given a Nyquist sampled discrete-time signal. By assuming, additionally, a value for the  $L$  parameter, the weighting matrix is computed by Eq.(25) and the PSD matrix estimate is obtained by means of Eq.(22).

## 5. Numerical assessment on extracting closely-spaced mode shapes from noisy signals

This section numerically assesses the potential of the multi-sensor PSBS approach proposed in Section 3 to discriminate closely-spaced and weakly excited vibrating modes from response acceleration signals corrupted by additive white noise which make up a challenging setting in OMA [2]. To this aim, a finite element space truss model is adopted, generating noiseless acceleration responses signals at Nyquist rate. Gaussian white noise of different intensity levels (i.e., signal-to-noise ratios, SNRs) is added to these signals. The noisy signals are multi-coset sampled using sampling schemes of various CRs and modal properties are obtained using the proposed PSBS approach in conjunction with the FDD. The obtained modal estimates are compared versus standard FDD applied to the Nyquist-sampled signals. The presentation starts with a description of the space truss structure and of the simulated Nyquist-sampled test signals.

### 5.1. Structural System description and computer-generated test signals

The aluminum space truss of Fig. 4 is adopted as a benchmark structure with geometry and properties purposely defined such that the first two modes of vibration along its gravitational axis are closely spaced. This 8-bay simply supported truss is modelled in a standard finite element (FE) software using 100 linear one-dimensional truss elements with circular hollow cross-sections. Each bay is a cube with 707mm long side. The horizontal truss elements in the x-y plane have 22mm

diameter and 1mm wall thickness, while the vertical truss elements in the x-z planes are 30mm in diameter and 1.5mm wall thickness. No diagonal members exist in the y-z plane rendering the truss susceptible to modal coupling (i.e., the two planar trusses on the x-z plane may vibrate almost independently along the z direction within their plane). Mass of 0.44kg is lumped at each of the 36 nodes of the FE model. Additional mass of 1.75kg is assigned to nodes 1,7,30, and 34, and of 2.75kg to nodes 20,26, and 32.

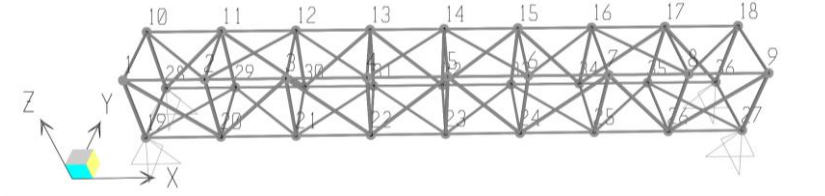


Fig. 4. Considered space truss model

The considered truss is assumed to be instrumented with an array of  $D=18$  wireless sensors placed at nodes 1-18 in Fig. 4, measuring vertical (i.e., along z-axis) acceleration responses under ambient wide-band stationary dynamic loading. A bandlimited low-amplitude Gaussian white noise force of 4s duration and a time discretization step equal to  $T_s=0.001s$  is applied at the base of the truss along the gravitational axis. Linear response history analysis is conducted for the above excitation assuming damping ratio of 1% for all modes to generate  $D=18$  vertical response acceleration discrete-time signals ( $x^a[v], x^b[v], a,b=\{1,2,\dots,18\}$ ), each consisting of 4000 samples associated with a Nyquist sampling rate at  $F_s= 1000Hz (= 1/0.001s)$ . For illustration, the signal recorded at node #5 of the truss in Fig. 4, is plotted in Fig.5(b). The considered excitation observes the PSD estimate shown in Fig.5(a) which has sufficient energy in the frequency range of up to 500Hz and can excite the first three bending modes of the space truss along the vertical direction (estimates of these mode shapes are shown later in Figs.7-9). Further, Fig.5(c) provides the PSD estimates of the generated truss acceleration response signals recorded at sensors #5 and #14 to illustrate differences to the frequency content among the test signals.

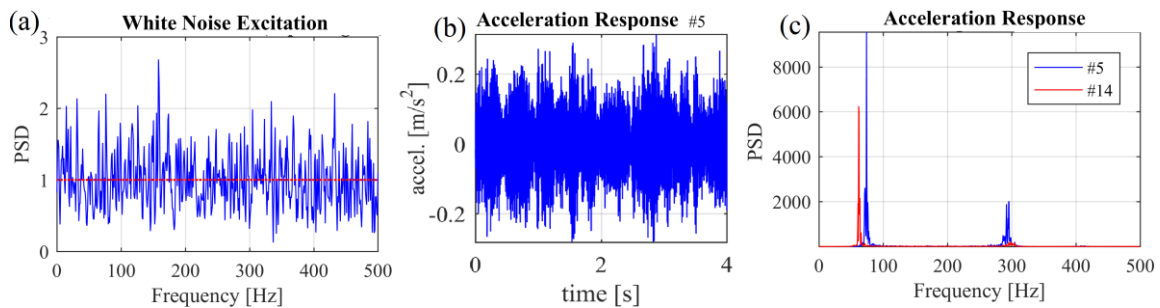


Fig. 5. Excitation and response data for the space truss in Fig. 4: (a) PSD estimate of white noise excitation; (b) Response acceleration at node #5; (c) PSD estimates of response acceleration at nodes #5 and #14. PSD estimates obtained by DFT-based Welch modified periodogram using 8 overlapping segments of the 4000-long signals with 50% overlap windowed by a Hanning function.

## 5.2. Application of multi-sensor PSBS

The above generated (noiseless) 18 response acceleration signals are contaminated with additive stationary Gaussian white noise at two different SNRs: 20dB, moderate noise case, and 0dB, extreme noise case in which the signal energy equals the noise energy. The noiseless and noisy signals are then multi-coset sampled at three different *CRs* approximately equal to 31%, 21% and 11% (i.e., 69%, 79% and 89% fewer samples compared to the Nyquist sampled full-length signals). These 3 different signal compression levels are achieved by adopting the  $(M,N)$  pairs of values reported in Table 1. Optimal sampling patterns are also reported in the same table along with the resulting compressed signal lengths. Note that the condition  $M^2 > N$  holds for the adopted  $(M,N)$  pairs ensuring that the  $\mathbf{R}_c$  matrix in Eq.(15) is full rank. Note further that the reason for not considering lower *CR* values in this study is because of practical/technological constraints as  $CR < 11\%$  can only be achieved by considering more than  $M=14$  parallel channels per sampler due to the  $M^2 > N$  condition, which is already a large number.

**Table 1** Design parameters of three different optimal multi-coset sampling schemes applied to response acceleration signals of the white noise excited truss example.

Compression Ratio/ Sub-Nyquist sampling rate	<i>CR</i>	31%	21%	11%
Number of channels per sensor	<i>M</i>	5	8	14
Down-sampling	<i>N</i>	16	39	128
Sampling pattern	<i>s</i>	[0,1,2,5,8]	[0,1,3,7,9,14,18,19]	[0,1,2,6,8,20,29,38,47,50,53,60,63,64]
Number of blocks	<i>K</i>	250	102	31
Nyquist sampled signals length	<i>KN</i>	4000	4000	4000
Sub-Nyquist sampled signals length	<i>KM</i>	1250	816	432
Design parameter <i>L</i>	<i>L</i>	20	8	2
Correlation support length	$N(2L+1)$	656	663	640

For exemplification, the case of the multi-coset sampling for  $CR=31\%$  is herein discussed to some detail. For  $CR=31\%$ , it is assumed that each of the 18 sensors used is equipped with the same multi-coset sampler comprising  $M=5$  channels, with each channel having an ADC unit operating at a rate  $N=16$  times slower than the Nyquist rate of 1000Hz. It is further assumed that all 18 samplers use the same sampling pattern at the 5 channels, given by the sequence  $\mathbf{s} = [0, 1, 2, 5, 8]^T$ . The latter has been obtained by solving the constrained optimization problem in Eqs. (28) and (29) for  $M=5$  and  $N=16$ . Following the details of multi-coset sampling in section 2, each Nyquist-sampled acceleration response signal is divided in  $K=250$  blocks of length  $N=16$  such that  $KN=4000$  Nyquist samples. From each block, only  $M=5$  samples are selected according to the above  $\mathbf{s}$  sequence (see also Fig. 2), resulting in the acquisition of  $KM=1250$  compressed samples per sensor. Similar calculations and considerations apply for the two multi-coset sampling cases with  $CR=21\%$  and  $CR=11\%$ .

Next, as shown in Fig. 3, the acquired *KM* compressed measurements from all 18 sensors are collectively processed to obtain an estimate of the output cross-correlation matrix  $\hat{\mathbf{r}}_{y^a y^b}$  in Eq. (13), based on Eq. (7) and the unbiased estimator  $\hat{\mathbf{r}}_{y_i^a y_j^b}[\ell]$  in (16). The latter is assumed to take on negligible values outside a range  $-L \leq \ell \leq L$ , where  $L$  is an integer user-defined parameter specified based on the desired resolution (or frequency domain discretization step  $\Delta\omega$ ) of the sought PSD-matrix estimate as discussed in section 3.2. In this regard, different  $L$  values reported in Table 1 are adopted for the three different *CRs* examined such that in all cases  $\Delta\omega = \frac{2\pi}{(2L+1)N} \approx 0.01$  rad/s. Once  $L$  is specified, the weighting matrix  $\mathbf{W}$  in Eq.(25) is computed and the PSD matrix estimate  $\hat{\mathbf{G}}_{x^a x^b}$  is obtained in Eq. (22) using the pattern correlation matrix  $\mathbf{R}_c$  in Eq. (15) along with the DFT matrix. For the particular case of  $CR=31\%$ ,  $\hat{\mathbf{r}}_{y^a y^b} \in \mathbb{R}^{1025 \times 18}$ ,  $\mathbf{R}_c \in \mathbb{R}^{1025 \times 656}$ ,  $\mathbf{W} \in \mathbb{R}^{M^2(2L+1) \times M^2(2L+1)}$ ,  $\mathbf{F}_{(2L+1)N} \in \mathbb{C}^{656 \times 656}$ , and  $\hat{\mathbf{G}}_{x^a x^b} \in \mathbb{C}^{656 \times 18}$  in Eq. (22).

### 5.3. PSBS-based FDD modal data estimation and assessment vis-à-vis non-compressive FDD

For all three *CRs* in Table 1 and different levels of noise, the standard peak-picking FDD algorithm relying on the SVD in Eq.(23) is employed to “decompose” the estimated PSD-matrix  $\hat{\mathbf{G}}_{x^a x^b}$  to its singular values,  $\mathbf{\Sigma}$ , and singular vectors,  $\mathbf{U}$ , as in Eq. (23), extracting estimates of the natural frequencies,  $\hat{f}_r$ , and mode shapes,  $\hat{\phi}_r$  of the truss in Fig. 4 corresponding to the  $r$ -th vertical vibration mode (PSBS-based FDD cases). Further, the FDD is also applied to the PSD matrix estimated from the Nyquist rate sampled signals (i.e.,  $CR=100\%$ ) discussed in Section 5.1 with and without additive noise using the Welch’s periodogram (see e.g., Fig. 5). Modal properties obtained from the noiseless non-compressed data are herein treated as the exact ones and used to assess the accuracy of the modal estimates  $\hat{f}_r$ ,  $\hat{\phi}_r$  obtained from the PSBS-based FDD cases.

Singular value vectors for all examined *CRs* for the noiseless ( $SNR=\infty$ ) and noisy signals with  $SNR=0$  dB are plotted in Fig. 6 in the frequency range of [0,500] Hz, where the first three resonant frequencies of the truss lie. They are normalized to unit amplitude to facilitate a comparison. It is seen that lower *CR* values (i.e., higher levels of data compression) yields less smooth plots. Still, even for the extreme case of  $CR=11\%$  the three prominent peaks corresponding to the three first resonant frequencies are discernible even for the  $SNR=0$  dB case (most clearly seen in the non-compressive case in the leftmost panels of Fig. 6) while their location on the frequency axis almost coincide with the those of the non-compressive case ( $CR=100\%$ ). This is true for both the first two closely-spaced

natural frequencies (i.e., their values differ only by about 15% while their difference is only 3% of the total frequency range considered up to 500Hz), as well as for the third natural frequency whose amplitude is significantly smaller than the first two as the third vibrating mode is weakly excited by the forcing function in Fig.5(a).

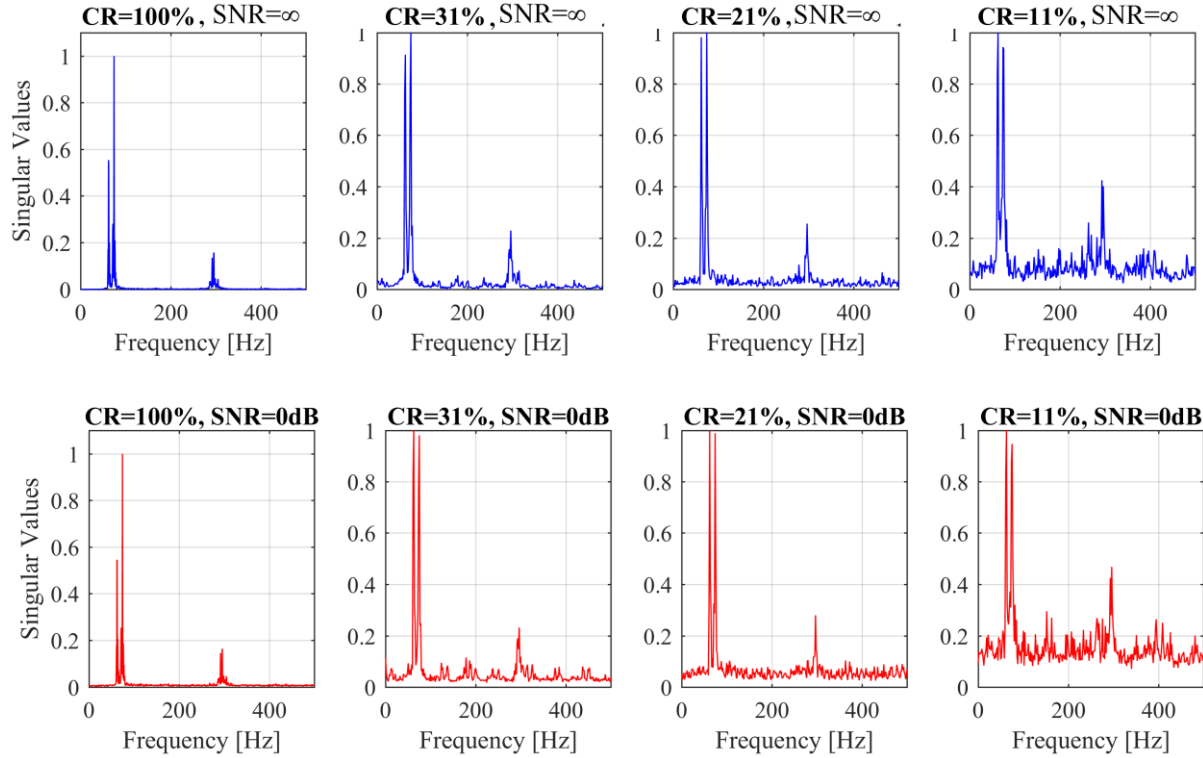


**Fig. 6.** Singular values vector of the truss in Fig. 4 for different  $CR$  values for the noiseless (upper row of panels) and for the noisy signals with  $SNR=0dB$  (lower row of panels).

The above observations are quantitatively verified in Table 2 which collects the natural frequencies obtained from singular values vectors and reports the difference percentage error,  $(\hat{f}_r - f_r)/f_r$  ( $r=1,2,3$ ), between the PSBS-based FDD estimates,  $\hat{f}_r$ , and the non-compressive FDD estimates,  $f_r$  for noiseless and noisy signals. Interestingly, it is seen that this error is independent of  $CR$  and  $SNR$  values: larger compression and more severe additive noise does not necessarily lead to less accurate natural frequency estimates. Importantly, in most cases considered, error differences in the natural frequencies is of the order of 1% demonstrating the potential of the proposed multi-sensor PSBS method to detect closely-spaced natural frequencies as well as weakly excited modes at  $CR$ s as low as 11% and with  $SNR$ s as low as 0 decibel (i.e., extreme high noise level).

**Table 2.** Natural frequency estimates and error differences  $(\hat{f}_r - f_r)/f_r$  ( $r=1,2,3$ ) in parentheses for the truss structure in Fig. 4.

Modal frequency	SNR [dB]	Non-compressive FDD		PSBS-based FDD	
		CR=100%	CR=31%	CR=21%	CR=11%
1 <sup>st</sup> natural frequency	$\infty$ (noiseless)	$f_1=62.012$ Hz (exact)	$\hat{f}_1=62.691$ Hz (1.10%)	$\hat{f}_1=62.121$ Hz (0.18%)	$\hat{f}_1=62.696$ Hz (1.10%)
	20	$f_1=63.965$ Hz (3.15%)	$\hat{f}_1=63.965$ Hz (3.15%)	$\hat{f}_1=63.965$ Hz (3.15%)	$\hat{f}_1=63.965$ Hz (3.15%)
	0	$f_1=61.035$ Hz (-1.57%)	$\hat{f}_1=62.691$ Hz (1.10%)	$\hat{f}_1=62.121$ Hz (0.18%)	$\hat{f}_1=62.696$ Hz (1.10%)
2 <sup>nd</sup> natural frequency	$\infty$ (noiseless)	$f_2=74.219$ Hz (exact)	$\hat{f}_2=74.924$ Hz (0.95%)	$\hat{f}_2=74.242$ Hz (0.03%)	$\hat{f}_2=73.668$ Hz (-0.74%)
	20	$f_2=74.219$ Hz (0%)	$\hat{f}_2=74.219$ Hz (0%)	$\hat{f}_2=74.219$ Hz (0%)	$\hat{f}_2=74.219$ Hz (0%)
	0	$f_2=74.219$ Hz (0%)	$\hat{f}_2=74.924$ Hz (0.95%)	$\hat{f}_2=74.242$ Hz (0.03%)	$\hat{f}_2=75.235$ Hz (1.37%)
3 <sup>rd</sup> natural frequency	$\infty$ (noiseless)	$f_3=295.898$ Hz (exact)	$\hat{f}_3=296.636$ Hz (0.25%)	$\hat{f}_3=296.970$ Hz (0.36%)	$\hat{f}_3=293.103$ Hz (-0.94%)
	20	$f_3=291.99$ Hz (-1.32%)	$\hat{f}_3=291.99$ Hz (-1.32%)	$\hat{f}_3=291.992$ Hz (-1.32%)	$\hat{f}_3=291.992$ Hz (-1.32%)
	0	$f_3=291.99$ Hz (-1.32%)	$\hat{f}_3=296.636$ Hz (0.25%)	$\hat{f}_3=296.970$ Hz (0.36%)	$\hat{f}_3=296.238$ Hz (0.11%)

Furthermore, modal deflected shapes of the truss in Fig. 4 are shown in Fig. 7-Fig. 9 extracted from the FDD method using Nyquist-sampled data (i.e., left figure panels case  $CR=100\%$ , non-compressive FDD) and compressed data at the highest compression level considered (i.e.,  $CR=11\%$ ) for both noiseless ( $SNR=\infty$ ) and noisy signals at  $SNR=\{20,0\}$ dB. With the exception of the first two closely-spaced modes at  $SNR=0$ dB, the remaining cases observe PSBS-based mode shape estimates that closely approximates those derived from noiseless Nyquist-sampled data which are treated hereafter as “exact”. Moreover, the accuracy of the proposed PSBS-based FDD approach in extracting quality estimates is quantitatively assessed with the Modal Assurance Criterion (MAC) [2], i.e.,

$$MAC(\phi, \hat{\phi}) = \frac{|\phi^T \hat{\phi}|^2}{\|\phi\|_2^2 \|\hat{\phi}\|_2^2} \quad (30)$$

which is a global measure of similarity between the exact  $\phi$  mode shape vectors (non-compressive FDD) and the estimated  $\hat{\phi}$  vectors (PSBS-based FDD). Perfect matching (similarity) is inferred for  $MAC=1$ , while  $MAC=0$  implies no matching. The criterion  $MAC > 0.9$  is commonly adopted as a good quality mode shape estimation indicator. The computed MAC values for  $SNR=\{\infty, 20, 0\}$  dB are

plotted in Fig. 10 as a function of the signal compression level. As intuitively expected, MAC values increase with  $CR$ , suggesting higher accuracy in the extracted mode shapes as more data samples are acquired. It is further seen that the quality of the modal estimates is not significantly affected by additive noise for SNR values above 20dB, yielding approximately the same high MAC values ( $>0.9$ ) as in the noiseless setting even for  $CR=11\%$  (i.e., 89% fewer measurements compared to the Nyquist rate). On the contrary, the combination of extreme noise level at  $SNR=0\text{dB}$  and high signal compression at  $CR=11\%$  adversely affects the detection of the underlying mode shapes of the truss, especially in the first two closely-spaced modes that attain MAC values well below the threshold of 0.9. Overall, the herein reported data illustrate the efficacy of the proposed method to address the modal coupling effect and identify weakly excited modes of vibration using noisy compressed signals at  $CR$  as low as 11% provided that the signal-to-noise ratio is not below 20dB.

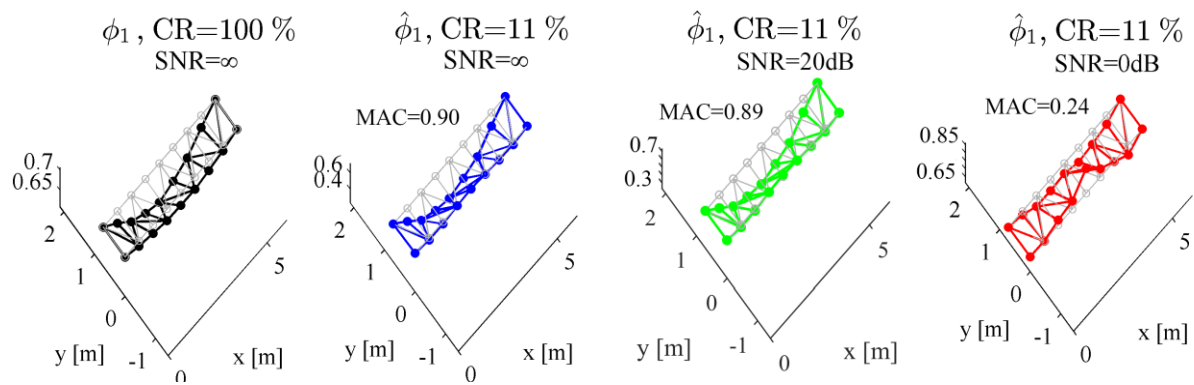


**Fig. 7.** Estimation of the 1<sup>st</sup> bending mode shape of the space truss for non-compressive FDD at  $CR=100\%$  and PSBS-based FDD at  $CR=11\%$  for  $SNR=\{\infty, 20, 0\}$  dB.

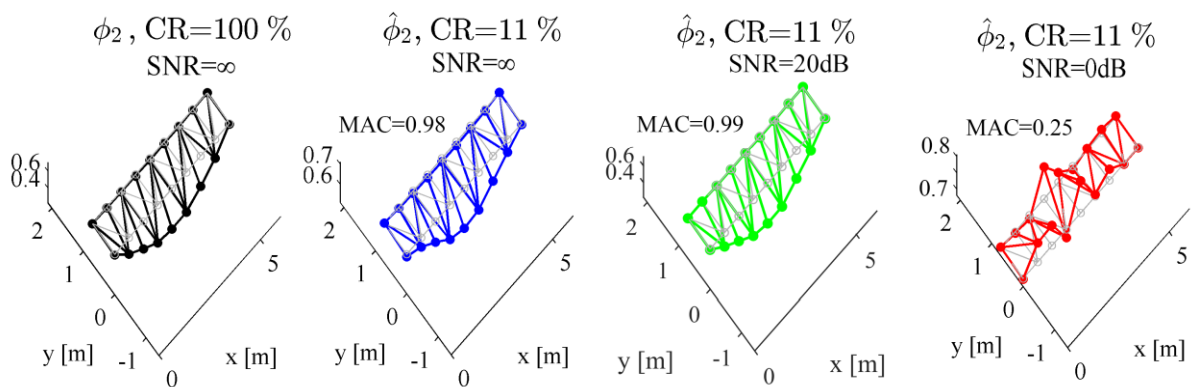


**Fig. 8.** Estimation of the 2<sup>nd</sup> bending mode shape of the space truss for non-compressive FDD at  $CR=100\%$  and PSBS-based FDD at  $CR=11\%$  for  $SNR=\{\infty, 20, 0\}$  dB.

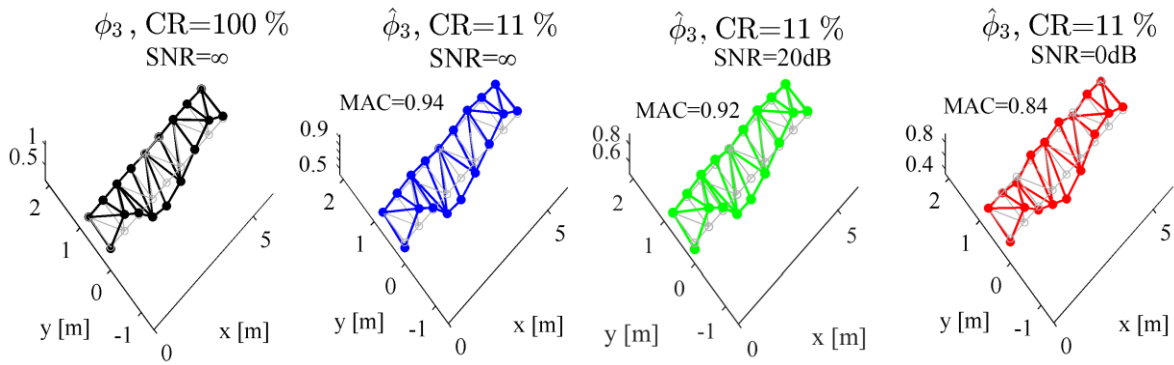


**Fig. 9.** Estimation of the 3<sup>rd</sup> bending mode shape of the space truss for non-compressive FDD at CR=100% and PSBS-based FDD at CR=11% for SNR={ $\infty$ , 20, 0} dB.

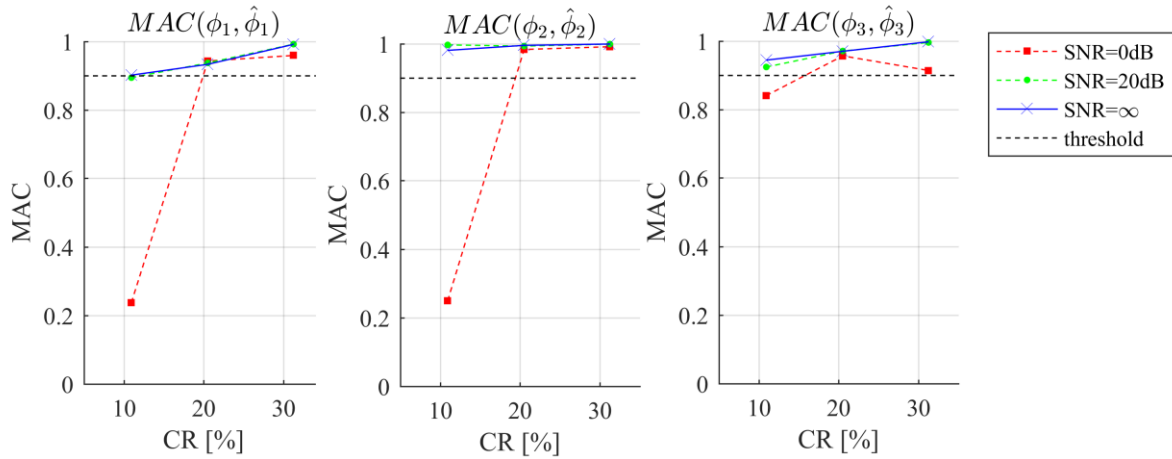


**Fig. 10.** MAC values of mode shapes as function of CR for SNR={ $\infty$ , 20, 0} dB.

## 6. Numerical assessment on mode shape estimation from field recorded data

In this section, the effectiveness of the multi-sensor PSBS method is further assessed against field recorded response acceleration data obtained from the Bärenbohlstrasse overpass in Zurich, Switzerland [36],[37] under operational conditions. The presentation begins by a short description of the structure and of the considered data and pre-processing before showcasing numerical results of the proposed method and comparisons with standard (non-compressive) FDD.

### 6.1. Structural system description and field recorded signals

The considered bridge is 30.90m long, having a deck of variable width, while it is almost symmetric along the longitudinal direction. It consists of a solid prestressed-slab with two equal-length spans of 14.75m each. The deck is supported, via steel bearings, in all directions at mid-span and in one of the abutments. The second abutment supports the deck only in the vertical and transverse directions. The bottom face of the deck was permanently instrumented with a network of

$D=18$  tethered sensors (i.e., Gantner Q-series DAQ devices equipped with anti-aliasing filter at a cut-off frequency of 50Hz [37]), measuring vertical acceleration response signals under operational conditions (e.g., wind, traffic, etc.) within a period of 12 months (from 12/7/2013 to 26/7/2014). In this respect, datasets of 18 vertical acceleration responses were acquired for approximately 10 minutes every hour with a sampling frequency of  $F_s=200\text{Hz}$  ( $T_s=0.005\text{s}$ ), using a conventional uniform sampling scheme. A sketch of the sensors layout is shown in Fig. 11, including the relative distances of the sensors in both horizontal dimensions. Further details regarding the bridge, the sensors installation, and data acquisition can be found in [36],[37].

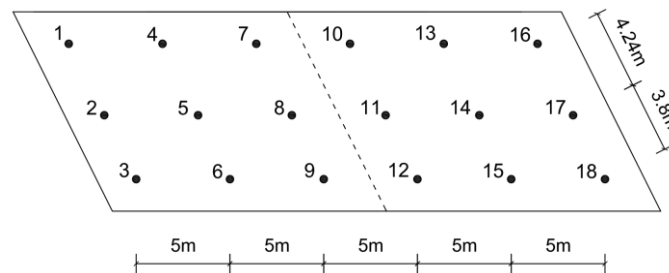


**Fig. 11.** Layout of the 18 sensors recording vertical acceleration responses under ambient excitation on the Bärenbohlstrasse bridge, Zurich, Switzerland [36],[37]

Herein, a dataset recorded on the 19/06/2014 at 15:08pm is considered comprising 18 vertical discrete-time acceleration response signals with duration equal to 2minutes. Signal pre-processing operations are applied to the raw dataset, which is down-sampled to the Nyquist sampling frequency at  $F_{NYQ}=100\text{Hz}$  ( $T_s=0.01\text{s}$ ), i.e., twice the upper cut-off frequency of the anti-aliasing filter [38]. The derived full-length/Nyquist-sampled signals (of 12000 samples each) are then processed with a 4<sup>th</sup>-order Butterworth band-pass filter in the frequency range [0.15, 50] in Hz to remove any potential low-frequency trend (below 0.15 Hz) from each acceleration response signal. For illustration, Fig. 12 presents the band-pass filtered acceleration responses signal recorded at sensor #13, together with its PSD estimate obtained from application of the Welch's periodogram.

Given that the PSBS-based spectral estimation approach anticipates signal stationarity which may not be the case for the considered signals since the bridge was open to the traffic during monitoring, it was deemed essential to undertake a data qualification test to appraise the stationarity of the recorded signals. To this end, the standard non-parametric Reverse Arrangement method (RAM) [39] is used to statistically test the stationarity hypothesis. The outcome of application of RAM to the signal is plotted in the right panel of Fig. 12. demonstrating that the stationarity hypothesis holds well within a 95% confidence interval. Similar outcomes have been obtained for the rest of the signals in the considered dataset and, therefore, the PSBS approach is applicable.

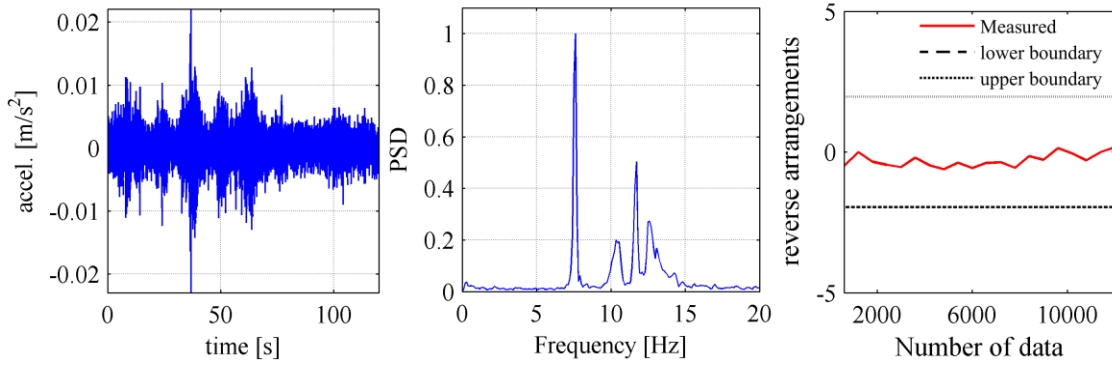


**Fig. 12.** Filtered acceleration response signal at sensor #13 (left), Welch modified periodogram of signal with 50% overlapping segments windowed by a Hanning function (right), reverse arrangement method results for signal windowed to 1min of duration (right).

### 6.2. Multi-sensor PSBS-based FDD and modal results

The above filtered dataset of field recorded signals are first multi-coset sampled using the same three sampling schemes as in Section 5.2. Table 3 reports all pertinent sampling parameters and achieved signal lengths. In this case, the values of the parameter  $L$  are chosen for each sampling

scheme to achieve  $\Delta\omega = \frac{2\pi}{(2L+1)N} \approx 0.005$  rad/s.

**Table 3** Design parameters of three different optimal multi-coset sampling schemes applied to recorded acceleration signals of the Bärenbohlstrasse bridge example.

Compression Ratio/ Sub-Nyquist sampling rate	CR	31%	21%	11%
Number of channels per sensor	$M$	5	8	14
Down-sampling	$N$	16	39	128
Sampling pattern	$s$	[0,1,2,5,8]	[0,1,3,7,9,14,18,19]	[0,1,2,6,8,20,29,38,47,50,53,60,63,64]
Number of blocks	$K$	750	307	93
Full-length/ Nyquist-sampled signals ( $F_s=100$ Hz)	$KN$	12000	12000	12000
Sub-Nyquist sampled signals length	$KM$	3750	2456	1302
Design parameter $L$	$L$	40	16	4
Correlation support length	$N(2L+1)$	1296	1287	1152

Next, the FDD algorithm is applied to PSD matrix estimates obtained from the sub-Nyquist multi-coset sampled signals at the three considered CRs in Table 3 as well as to the PSD matrix obtained from the filtered Nyquist-sampled signals using Welch's periodogram. The derived singular values vector in Eq. (23) are shown in Fig. 13 normalized to their maximum value. It is seen that 4 prominent peaks (i.e., natural frequencies) exist corresponding to the lowest four flexural vibration modes along the vertical axis of the bridge (plotted later in Figs. 13-16). The highest singular value amplitudes are observed at the first and third vibrating modes which are mostly excited (see also middle panel of Fig. 12) and accurately captured by the PSBS-based FDD approach even for CR= 11%.

The second and fourth modes are weakly excited rendering their detection as a more challenging task. In fact, the quality estimate of the least excited vibration mode (i.e., the 4<sup>th</sup> resonance) is adversely affected at the highest signal compression level considered (i.e.,  $CR=11\%$ ), but this issue is significantly rectified for  $CR \geq 21\%$ .

Regarding the natural frequency estimation problem, the above observations are qualitatively assessed in Fig. 13 and quantified in Table 4 using the error differences between the “exact” natural frequency values extracted from the non-compressed signals ( $CR=100\%$ ) and the natural frequency estimates of the compressive PSBS-based FDD approach. A maximum error of 2.32% occurs for  $CR=21\%$  in estimating the 2<sup>nd</sup> resonance while the remaining errors are lower than 1%.

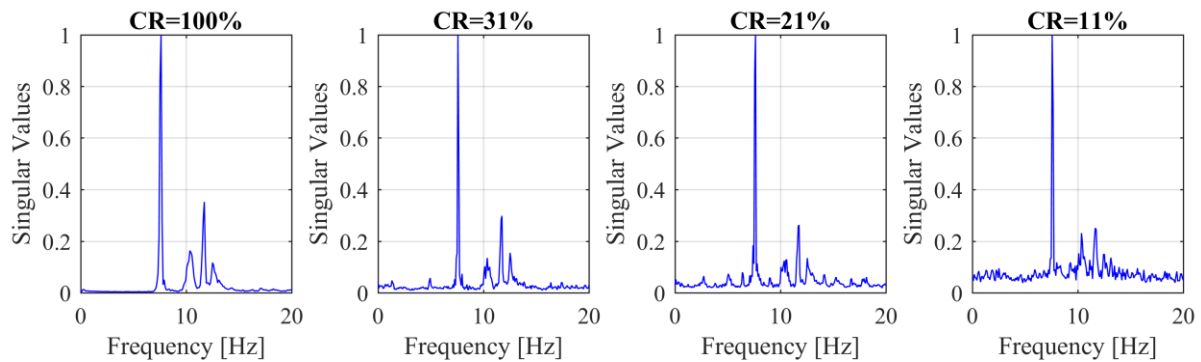


**Fig. 13.** First singular values vector of the bridge response spectrum matrix in Eq. (22) for  $CR=31\%$  (left),  $CR=21\%$  (middle), and  $CR=11\%$  (right)

**Table 4.** Natural frequency estimates and error differences  $(\hat{f}_r - f_r) / f_r$  ( $r=1,2,3,4$ ) in parentheses for Bärenbohlstrasse bridge.

Non-compressive FDD	PSBS-based FDD		
$CR=100\%$	$CR=31\%$	$CR=21\%$	$CR=11\%$
$f_1 = 7.617$ Hz	$\hat{f}_1 = 7.573$ Hz (-0.57%)	$\hat{f}_1 = 7.632$ Hz (0.20%)	$\hat{f}_1 = 7.565$ Hz (-0.68%)
$f_2 = 10.352$ Hz	$\hat{f}_2 = 10.355$ Hz (0.04%)	$\hat{f}_2 = 10.592$ Hz (2.32%)	$\hat{f}_2 = 10.348$ Hz (-0.04%)
$f_3 = 11.719$ Hz	$\hat{f}_3 = 11.747$ Hz (0.24%)	$\hat{f}_3 = 11.760$ Hz (0.35%)	$\hat{f}_3 = 11.652$ Hz (-0.57%)
$f_4 = 12.500$ Hz	$\hat{f}_4 = 12.519$ Hz (0.15%)	$\hat{f}_4 = 12.539$ Hz (0.31%)	$\hat{f}_4 = 12.522$ Hz (0.17%)

The extracted modal deflected shapes of the four vibrating modes are illustrated in Fig. 14-Fig. 17. The left panels in these figures present the “exact” mode shapes pertaining to non-compressive FDD while the middle panels depict the modal shapes estimated from the proposed PSBS-based FDD at  $CR=11\%$ . Their accuracy is assessed with the MAC in Eq. (30), which is plotted in the right panels of Fig. 14-Fig. 17 as a function of the three adopted  $CR$ s.

It is seen that accurate mode shapes with  $MAC$  values equal or above 0.9 are obtained for the

first three modes even for the lowest CR, which reflects a slower sampling at 89% below Nyquist that collects only 1302 data samples from each sensor within 2 minutes out of the 12000 samples in the full-length signals. Regarding the fourth and least excited vibration mode, fairly accurate estimates are retrieved for  $CR \geq 21\%$ , but this mode is not accurately resolved at higher signal compression levels (i.e.,  $CR=11\%$ ), yielding very low MAC values. Overall, the herein reported results demonstrate the effectiveness of the multi-sensor PSBS-based approach to identify mode shapes and natural frequencies of the monitored bridge from recorded data without being significantly affected from signal compression as long as modes are sufficiently excited.

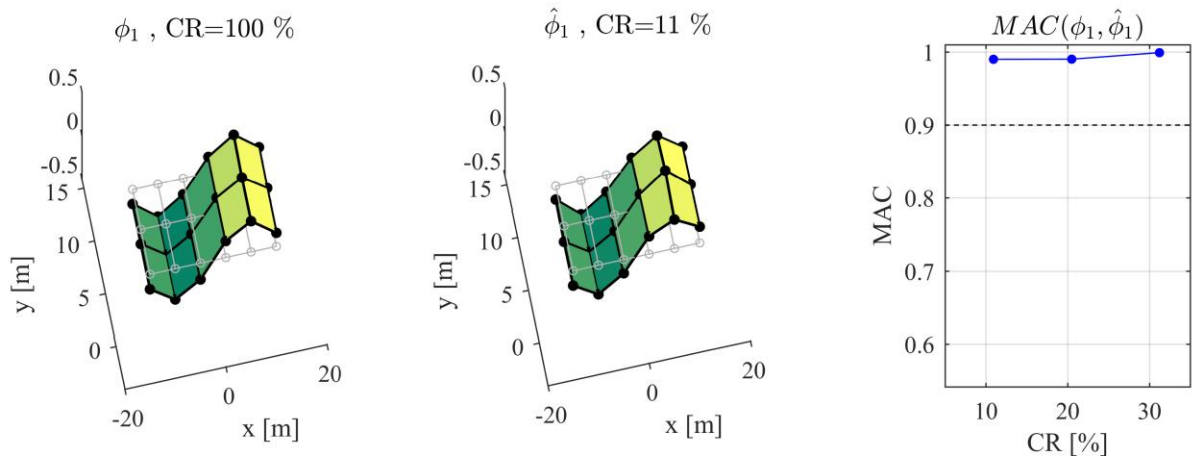


**Fig. 14.** Estimation of the 1<sup>st</sup> mode shape (bending) of the Bärenbohlstrasse bridge; non-compressive FDD (left); PSBS-based FDD at  $CR=11\%$  (middle); and MAC values versus CR (right)

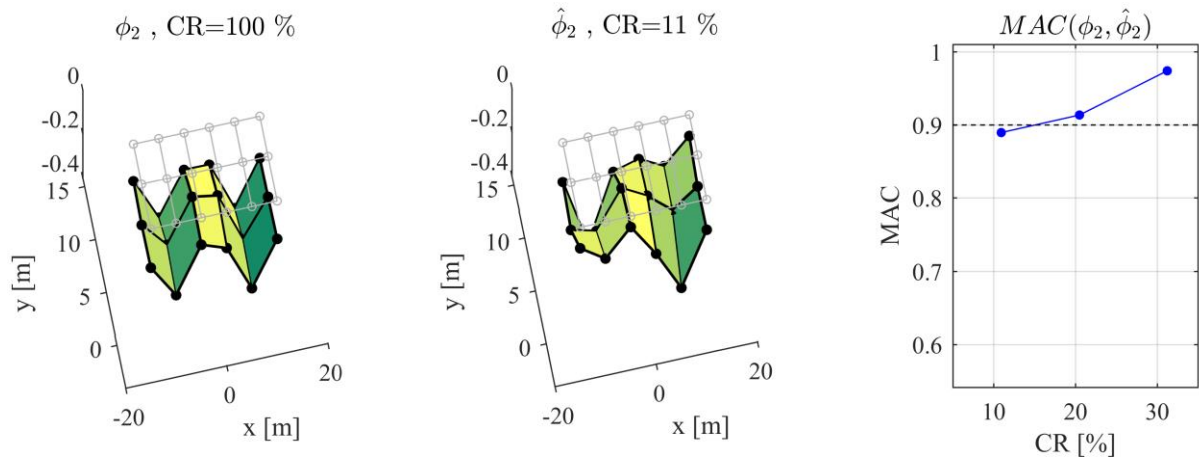


**Fig. 15.** Estimation of the 2<sup>nd</sup> mode shape (bending) of the Bärenbohlstrasse bridge; non-compressive FDD (left); PSBS-based FDD at  $CR=11\%$  (middle); and MAC values versus CR (right).

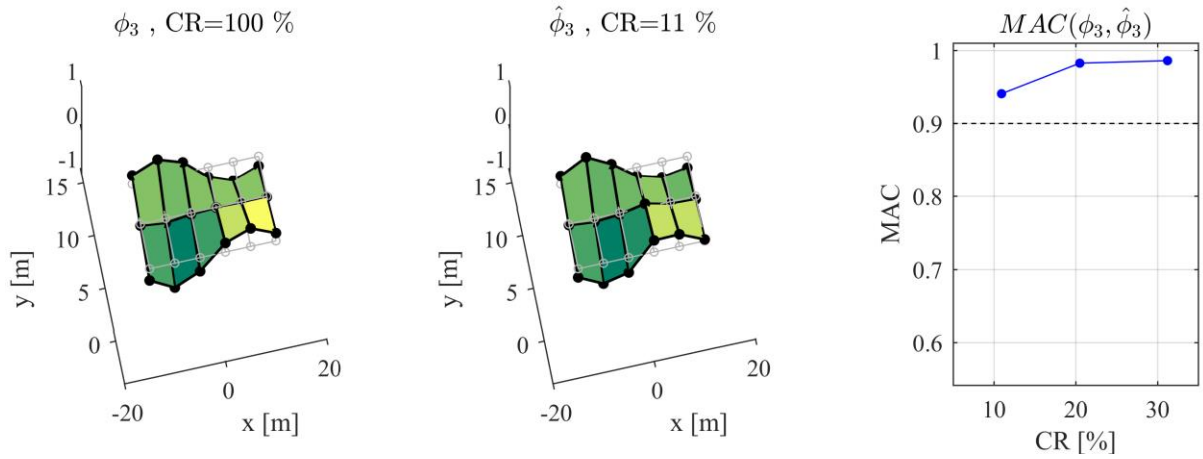


**Fig. 16.** Estimation of the 3<sup>rd</sup> mode shape (rotational) of the Bärenbohlstrasse bridge; non-compressive FDD (left); PSBS-based FDD at CR=11% (middle); and MAC values versus CR (right).

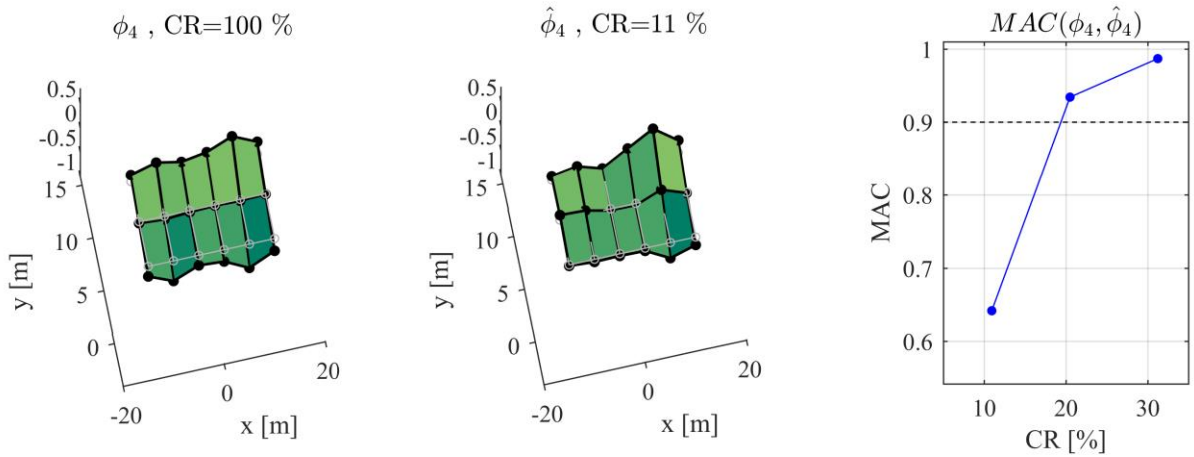


**Fig. 17.** Estimation of the 4<sup>th</sup> mode shape (rotational) of the Bärenbohlstrasse bridge; non-compressive FDD (left); PSBS-based FDD at CR=11% (middle); and MAC values versus CR (right).

## 7. Estimation of battery life gain in wireless sensors employing multi-coset samplers for PSBS-based OMA

In this section, daily energy consumption and battery lifetime are estimated for a wireless sensor assumed to be part of an array of sensors monitoring the bridge considered in Section 6.1. The aim is to quantify savings in energy consumption and battery lifetime achieved by the reduced sampling and wireless data transmission rates enabled by the proposed multi-sensor PSBS approach with multi-coset sampling (Fig. 1-bottom chart) vis-à-vis conventional sampling with and without off-line compression (Fig. 1-top chart). To this aim, a star network topology of equidistant wireless

sensors is assumed, measuring 2minutes long vertical bridge response acceleration signals under operational conditions every hour (i.e., a dataset of  $Q=24$  acceleration signals are collected daily per wireless sensor). Energy consumption estimates are computed for the three different multi-coset sampling schemes in Table 3, considering samplers with  $M$  ADC units operating at the sub-Nyquist sampling rates. In active mode, it is assumed that all  $M$  ADC units sample concurrently followed by wireless data transmission. Power requirements of the considered wireless sensor in idle and active operating modes are listed in Table 5 as well as the current drawn in each mode assuming a supply voltage of 3V. These figures have been adopted from the specifications of a typical conventional wireless sensor, namely WiseNode v4, developed by Novakovic et al. [40].

**Table 5** Wireless Sensor WiseNode v4 specifications [40]

Mode	Current Drawn	Power Consumption
Idle	27 $\mu$ A	$P_I= 81 \mu$ W
Sampling	Variable	$P_s= E_s/T_s$ ( $E_s=55.3 \mu$ J)
ADC	0.72 mA	$P_{ADC}= 2.16$ mW
Transmit	34.6 mA	$P_T= 103.8$ mW

Daily energy demands for a single sensor,  $E_{tot}$ , are calculated separately for each operating mode (i.e., sampling and ADC, wireless transmission, and idle), taking that multi-coset-based sampling is undertaken for the three sampling schemes in Table 3 (i.e.,  $CR= 31\%$ ,  $21\%$  and  $11\%$ ). Numerical results of the pertinent calculations are reported in the three rightmost columns of Table 6. For illustration, the case of  $CR=11\%$  is discussed in detail. The considered multi-coset sampler comprises  $M=14$  channels, each operating at a sampling rate of  $T_{s,CR}=1.28s$ , that is  $N=128$  times slower than the original conventionally sampled data at  $T_s=0.01s$  (i.e.,  $F_s=100Hz$ ). Power consumption due to sampling is determined as  $P_{s,CR} = M \cdot (E_s / T_{s,CR}) = 0.60$  mW, using the  $E_s$  value given in Table 5. Therefore, the daily acquisition of  $Q=24$  compressed acceleration responses of  $N_{L,CR}=1302$  samples each, requires that the sensor operates in sampling mode for  $t_s=Q \cdot (N_{L,CR}/M) \cdot T_{s,CR} \approx 2860s$  (or 0.8h), consuming  $E_{s\&ADC} = (P_{s,CR} + P_{ADC}) \cdot t_s \approx 7.96J$  of energy per day for combined sampling and ADC. Assuming next that each ADC unit has a resolution of 16 bits (i.e., 2 bytes), then  $I_{FWD} \approx 2625$  bytes of data package information are generated per compressed acceleration sequence, which are wirelessly transmitted to the server within a time frame of  $t_{FWD} = (I_{FWD} / I_{T1}) \cdot t_{T1} \approx 7.61s$ , where  $I_{T1}=7$  bytes is the information carried within one data package and  $t_{T1}= 0.02s$  is the time required for its wireless transmission [40]. Thus,  $t_T = Q t_{FWD} = 182.6s$  (or 0.05h) are required for the daily transmission of the  $Q=24$  sequences of compressed acceleration response data, consuming  $E_T = P_T \cdot t_T = 18.95J$  of energy per day. The adopted wireless sensor is assumed to be in the idle mode for the remaining  $t_I =$

24 -  $t_\tau - t_s = 23.15\text{h}$  (or  $t_\tau = 83340\text{s}$ ) of the day using  $E_i = P_i \cdot t_i = 6.75\text{J}$  of energy. Therefore, overall, the daily sensor energy consumption for the  $CR=11\%$  case is  $E_{tot} = E_{s\&ADC} + E_T + E_i = 33.67\text{J}$  as reported in Table 6. Similar calculations have been performed to estimate  $E_{tot}$  for  $CR=21\%$  and  $31\%$  and results are shown in Table 6. Moreover, for the sake of comparison, the same table includes pertinent results obtained for two additional cases in which sensors sample uniformly in time the  $Q=24$  response acceleration signals per day at the original rate of  $T_s=0.01\text{s}$  and, then, one performs off-line lossless signal compression using Huffman coding at  $CR=77.6\%$  [8], while the second transmits full-length signals (i.e.,  $CR=100\%$ ). Note that the latter case, whilst practically not realistic, is the one most widely considered in the literature in comparative studies on energy savings quantification in wireless sensors (e.g., [13],[14],[18]). Note also that  $CR=77.6\%$  is a typical value that Huffman coding, as well as other lossless off-line data compression techniques, may achieve.

**Table 6** Daily energy consumption and battery life estimates for various  $CR$  values

Mode	Conventional sampling				Compressed multi-coset sampling					
	$CR=100\%$ (No compression before transmission)		$CR=77.6\%$ (Off-line lossless compression before transmission)		$CR=31\%$		$CR=21\%$		$CR=11\%$	
	Time [h]	Energy [J]	Time [h]	Energy [J]	Time [h]	Energy [J]	Time [h]	Energy [J]	Time [h]	Energy [J]
Idle	22.74	6.63	22.84	6.66	23.06	6.72	23.10	6.74	23.15	6.75
Sampling & ADC	0.80	22.15	0.80	22.15	0.80	11.20	0.80	9.49	0.80	7.96
Transmit	0.46	173.29	0.36	134.48	0.14	54.15	0.10	35.55	0.05	18.95
<b><math>E_{tot}</math> [J]</b>	-	<b>202.07</b>	-	<b>163.28</b>	-	<b>72.08</b>	-	<b>51.77</b>	-	<b>33.67</b>
<b><math>T_b</math> [years]</b>	-	<b>0.87</b>	-	<b>1.08</b>	-	<b>2.40</b>	-	<b>3.31</b>	-	<b>5.0</b>

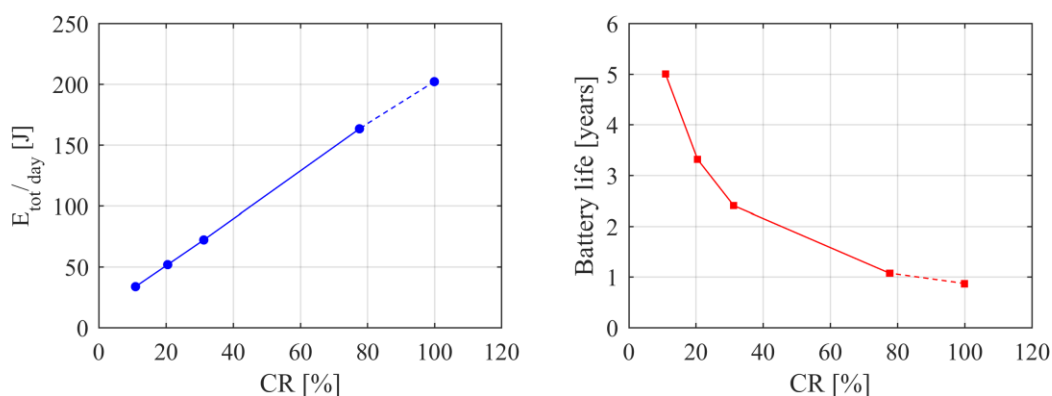


**Fig. 18.** Estimates of the total energy requirements (left) and the battery life (right) for different  $CR$  values for a single wireless sensor monitoring the Bärenbohlstrasse bridge of Section 6.1.

Focusing on the numerical values shown in Table 6, it is seen that significant estimated total energy savings,  $E_{tot}$ , are found as  $CR$  reduces, following an overall linear relationship as can be appreciated by the  $E_{tot}$  versus  $CR$  plot in the left panel of Fig. 18. The practical importance of the

above savings in energy consumption achieved by the proposed approach can be appreciated by quantifying their influence to battery lifetime. To this aim, it is assumed that the sensor energy supply of 3V comes from two Energizer L91 AA-size lithium batteries with a nominal voltage of  $V_n=1.5V$  and a capacity of  $C_n=3000$  mAh, providing a total energy of  $E_b= (2C_n)\cdot(2V_n)= 64800J$ . A continuous discharge current is further assumed to occur across the lifetime of the battery, pertaining to an annual battery energy loss due to leakage expressed in the percentage ratio of  $\xi=1\%$ . In this respect, the following expression can be used

$$T_b = \frac{E_b}{E_{tot} + \xi \cdot E_b}, \quad (31)$$

to estimate sensor battery life  $T_b$ . The latter quantity is computed for all 5 different wireless sensors considered before in the last row of Table 6 and is further plotted against  $CR$  in the right panel of Fig. 18. Clearly, the battery life expectancy increases exponentially with lower  $CR$ s. Specifically, battery life triples for  $CR=21\%$  compared to Nyquist sampling, while  $CR=11\%$  prolongs battery lifetime up to 5 times. In this respect, the proposed PSBS approach for OMA can support an overall sustainable bridge monitoring system with reduced maintenance costs associated with labor expenses and/or interruption of the normal operation of the monitored bridge since battery replacement can be scheduled at longer intervals.

## **8. Concluding remarks**

A novel centralized multi-sensor approach for OMA of engineering structures has been proposed supporting the use of low-power wireless sensor networks acquiring response acceleration measurements at sub-Nyquist rates. The proposed approach relies on deterministic non-uniform in time multi-coset sampling along with a PSBS technique, herein extended to the multi-sensor regime, to estimate the response acceleration PSD matrix of linear structures vibrating under broadband stationary random excitation. The estimated PSD matrix is decomposed to its singular values and vectors to retrieve mode shapes and natural frequencies using the standard peak-picking FDD algorithm.

The assumption of having identical multi-coset samplers in all sensors of the WSN functioning under the same multi-coset sampling sequences has been made in the problem formulation to facilitate practicality in implementation. Further, the multi-coset sampling sequences have been optimally designed for sampling constant (white noise) PSD function corresponding to least sparse stationary random processes acquired at a single sensor. The latter consideration reinforces the spectral agnostic attribute of the proposed PSBS-based OMA approach. This attribute has allowed for treating stationary signals of arbitrary frequency content without requiring prior knowledge of

their spectral support.

The efficacy of the proposed method has been numerically demonstrated by considering two different sets of Nyquist sampled discrete-time signals compressed at various compression levels using different multi-coset sampling sequences. The first set of signals were computer-simulated acceleration responses, noiseless and with additive Gaussian white noise, pertaining to a white-noise excited FE space truss with two closely-spaced modes of vibration. The second set of signals were two-minute long field-recorded acceleration response time-histories recorded during a monitoring campaign of a particular overpass subject to operational dynamic loading. Based on the MAC criterion, it was shown that accurate mode shape identification can be achieved for up to almost 90% slower than Nyquist sampling rates for sufficiently excited modes and/or as long as noise does not exceed  $\text{SNR}=20\text{dB}$ . For more severely noise corrupted signals with  $\text{SNR}=0\text{dB}$  and/or for the least excited modes of the bridge, good quality mode shape estimates were achieved for up to about 80% below Nyquist sampling rate. Lastly, longer battery lifetime by about 3 and 5 times compared to conventional Nyquist sampling has been estimated for multi-coset sampling at rates 80% and 90% below Nyquist, respectively, based on power requirement specifications of a typical commercially available wireless sensor assumed to have multi-coset signal acquisition capabilities.

Collectively, the above quantitative findings derived from the herein furnished numerical data suggest that the proposed approach may significantly reduce maintenance costs in WSNs leading to cost-effective and sustainable OMA deployments once wireless sensors equipped with multi-coset samplers become commercially available. Moreover, the proposed approach supports simultaneous data acquisition and compression at the sensor front-end, eliminating the need for local on-sensor data interrogation/processing which further minimizes sensor complexity and memory requirements. Still, the proposed approach involves two practically important prerequisites which may limit its applicability in certain monitoring scenarios: (i) it anticipates stationary signals and, therefore, treatment of non-stationary response acceleration signals either due to non-stationary excitation and/or nonlinear or time-varying structural behavior need to be carefully considered (e.g., through consideration of windowing in time to satisfy stationarity statistical tests with high probability); (ii) it does not return time-histories of response acceleration signals and, therefore, it is only relevant to structural health monitoring approaches relying on second-order response statistics as in the case of extracting modal information via frequency domain SVD-based OMA approaches. In this respect, further research is warranted to assess the effectiveness and applicability of the herein proposed approach vis-à-vis various sub-Nyquist CS-based approaches for OMA not limited by the above prerequisites in different practical structural health monitoring applications. Some pertinent results along these lines are reported in [27],[28]. Moreover, experimental verification of the

proposed approach in actual field deployments is left for future work as it requires the availability of currently non-existent acceleration wireless sensors equipped with multi-coset sampling capabilities. The development of such sensors is foreseeable in the near future based on recent advances in multi-coset sampling hardware addressing problems such as channel diversity gain, time-synchronization, and time-jittering arising in interleaved ADC architectures [33]-[35]. To this end, it is envisioned that the developed approach will motivate further research on sensors technology tailored for large-scale structural health monitoring applications.

### **Acknowledgements**

This work has been funded by EPSRC in UK, under grant No EP/K023047/1: the second author is indebted to this support. The first author further acknowledges the support of City, University of London through a PhD studentship. The authors gratefully acknowledge Prof. Eleni Chatzi and Dr Vasileios Dertimanis of ETH, Zürich for providing field recorded acceleration data of the Überführung Bärenbohlstrasse Bridge considered in Section 6.

### **References**

- [1] E. Reynders, System Identification Methods for (Operational) Modal Analysis: Review and Comparison, *Arch. Comput. Methods Eng.* 19 (2012) 51–124. doi:10.1007/s11831-012-9069-x.
- [2] R. Brincker, C.E. Ventura, *Introduction to Operational Modal Analysis*, John Wiley & Sons, Ltd, Chichester, UK, 2015. doi:10.1002/9781118535141.
- [3] J.P. Lynch, An overview of wireless structural health monitoring for civil structures, *Philos. Trans. R. Soc. A Math. Phys. Eng. Sci.* 365 (2007) 345–372. doi:10.1098/rsta.2006.1932.
- [4] J.P. Lynch, K.J. Loh, A Summary Review of Wireless Sensors and Sensor Networks for Structural Health Monitoring, *Shock Vib. Dig.* 38 (2006) 91–128. doi:10.1177/0583102406061499.
- [5] T. Nagayama, B.F.J. Spencer, Structural health monitoring using smart sensors, (2007) 186. <https://www.ideals.illinois.edu/handle/2142/3521>.
- [6] B.F. Spencer, C. Yun, *Wireless Sensor Advances and Applications for Civil Infrastructure Monitoring*, (2010).
- [7] M.F. Duarte, G. Shen, A. Ortega, R.G. Baraniuk, Signal compression in wireless sensor networks., *Philos. Trans. A. Math. Phys. Eng. Sci.* 370 (2012) 118–35. doi:10.1098/rsta.2011.0247.
- [8] J.P. Lynch, A. Sundararajan, K.H. Law, A.S. Kiremidjian, E. Carryer, Power-efficient data

- management for a wireless structural monitoring system, Proc. 4th Int. Work. Struct. Heal. Monit.(2003).<http://citeseerx.ist.psu.edu/viewdoc/download?doi=10.1.1.66.1672&rep=rep1&type=pdf>.
- [9] Y. Bao, J.L. Beck, H. Li, Compressive sampling for accelerometer signals in structural health monitoring, *Struct. Heal. Monit.* 10 (2011) 235–246. doi:10.1177/1475921710373287.
- [10] E.J. Candès, The restricted isometry property and its implications for compressed sensing, *Comptes Rendus Math.* 346 (2008) 589–592. doi:10.1016/j.crma.2008.03.014.
- [11] D.L. Donoho, Compressed sensing, *IEEE Trans. Inf. Theory.* 52 (2006) 1289–1306. doi:10.1109/TIT.2006.871582.
- [12] N. Vaswani, J. Zhan, Recursive Recovery of Sparse Signal Sequences from Compressive Measurements: A Review, *IEEE Trans. Signal Process.* 64 (2016) 3523–3549. doi:10.1109/TSP.2016.2539138.
- [13] S.M. O’Connor, J.P. Lynch, A.C. Gilbert, Compressed sensing embedded in an operational wireless sensor network to achieve energy efficiency in long-term monitoring applications, *Smart Mater. Struct.* 23 (2014) 85014. doi:10.1088/0964-1726/23/8/085014.
- [14] S.M. O’Connor, J.P. Lynch, A.C. Gilbert, Implementation of a compressive sampling scheme for wireless sensors to achieve energy efficiency in a structural health monitoring system, in: T.Y. Yu, A.L. Gyekenyesi, P.J. Shull, A.A. Diaz, H.F. Wu, A.E. Aktan (Eds.), *Proc. SPIE - Int. Soc. Opt. Eng.*, 2013: p. 86941L. doi:10.1117/12.2010128.
- [15] Y. Yang, S. Nagarajaiah, Output-only modal identification by compressed sensing: Non-uniform low-rate random sampling, *Mech. Syst. Signal Process.* 56–57 (2015) 15–34. doi:10.1016/j.ymssp.2014.10.015.
- [16] Y. Yang, C. Dorn, T. Mancini, Z. Talken, S. Nagarajaiah, G. Kenyon, C. Farrar, D. Mascarenas, Blind identification of full-field vibration modes for output-only structures from uniformly-sampled, possibly temporally-aliased (sub-Nyquist), video measurements, *J. Sound Vib.* 390 (2017) 232-256. doi: 10.1016/j.jsv.2016.11.034.
- [17] J.Y.. Park, M.B.. Wakin, A.C.. Gilbert, Modal analysis with compressive measurements, *IEEE Trans. Signal Process.* 62 (2014) 1655–1670. doi:10.1109/TSP.2014.2302736.
- [18] R. Klis, E. Chatzi, Data recovery via Hybrid Sensor Networks for Vibration Monitoring of Civil Structures, *Int. J. Sustain. Mater. Struct. Syst.* 2 (2015) 161–184.
- [19] R. Klis, E.N. Chatzi, Vibration monitoring via spectro-temporal compressive sensing for wireless sensor networks, *Struct. Infrastruct. Eng.* 13 (2017) 195–209. doi:10.1080/15732479.2016.1198395.
- [20] G. Leus, D.D. Ariananda, Power spectrum blind sampling, *IEEE Signal Process. Lett.* 18 (2011)

- 443–446. doi: 10.1109/LSP.2011.2158604.
- [21]D. Cohen, Y. Eldar, Sub-Nyquist Sampling for Power Spectrum Sensing in Cognitive Radios: A Unified Approach, *IEEE Trans. Signal Process.* 62 (2014) 3897–3910. doi:10.1109/TSP.2014.2331613.
- [22]D.D. Ariananda, G. Leus, Compressive Wideband Power Spectrum Estimation, *Signal Process. IEEE Trans.* 60 (2012) 4775–4789. doi:10.1109/TSP.2012.2201153.
- [23]M. Mishali, Y.C. Eldar, Blind Multiband Signal Reconstruction: Compressed Sensing for Analog Signals, *IEEE Trans. Signal Process.* 57 (2009) 993–1009. doi:10.1109/TSP.2009.2012791.
- [24]D.D. Ariananda, G. Leus, Cooperative compressive wideband power spectrum sensing, in: 2012 Conf. Rec. Forty Sixth Asilomar Conf. Signals, Syst. Comput., IEEE, 2012: pp. 303–307. doi:10.1109/ACSSC.2012.6489012.
- [25]R. Venkataramani, Y. Bresler, Optimal sub-Nyquist nonuniform sampling and reconstruction for multiband signals, *IEEE Trans. Signal Process.* 49 (2001) 2301–2313. doi:10.1109/78.950786.
- [26]B. Tausiesakul, N. Gonzalez-Prelcic, Power Spectrum Blind Sampling Using Minimum Mean Square Error and Weighted Least Squares, in: 47th Asilomar Conf. Signals, Syst. Comput. (ACSSC ), 2013: pp. 153–157.
- [27]K. Gkoktsi, A. Giaralis A, Assessment of sub-Nyquist deterministic and random data sampling techniques for operation modal analysis, *Struct. Health Monitor.* 16 (2017) 630-646. doi: 10.1177/1475921717725029.
- [28]K. Gkoktsi, A. Giaralis, R.P. Klis, V. Dertimanis, E.N. Chatzi, Vibration-based structural performance assessment via output-only sub-Nyquist/compressive wireless sensor data, in: Fourth Conf. Smart Monitor., Assess. Rehab. Civil Struct. (SMAR 2017), Zurich, Switzerland, 2017.
- [29]W.C. Black, D.A. Hodges, Time Interleaved Converter Arrays, *IEEE J. Solid-State Circuits.* 15 (1980) 1022–1029. doi:10.1109/JSSC.1980.1051512.
- [30]M. Mishali, Y.C. Eldar, From Theory to Practice : Sub-Nyquist Sampling of Sparse Wideband Analog Signals, *IEEE J. Sel. Top. Signal Process. Spec. Issue Compress. Sens.* 4 (2010) 375–391. doi:10.1109/JSTSP.2010.2042414.
- [31]T. Moon, H.W. Choi, N. Tzou, A. Chatterjee, Wideband Sparse Signal Acquisition with Dual-rate Time-Interleaved Undersampling Hardware and Multicoset Signal Reconstruction Algorithms, *IEEE Trans. Signal Process.* 63 (2015) 6486–6497. doi:10.1109/TSP.2015.2469648.

- [32]Z. Jingchao, L. Peizhuo, F. Ning, P. Xiyuan, Prototype design of multicore sampling based on compressed sensing, in: IEEE 12th Int. Conf. Electron. Meas. Instruments, Qingdao, Shandong, China., 2015: pp. 1303–1308.
- [33]R. Brincker, C.E. Ventura, P. Andersen, Damping estimation by frequency domain decomposition, in: 19th Int. Modal Anal. Conf. (IMAC), Kissimmee, FL, USA, 2001: 698–703.
- [34]R. Brincker, L. Zhang, Frequency domain decomposition revisited, in: third Int. Oper. Modal Anal. Conference (IOMAC), May 4–6, Ancona, p. 615–626, 2009.
- [35]D. Romero, D.D. Ariananda, Z. Tian, G. Leus, Compressive covariance sensing: Structure-based compressive sensing beyond sparsity, *IEEE Signal Process. Mag.* 33 (2015) 78-93. doi:10.1109/MSP.2015.2486805
- [36]M.D. Spiridonakos, E.N. Chatzi, B. Sudret, Polynomial Chaos Expansion Models for the Monitoring of Structures under Operational Variability, *ASCE-ASME J. Risk Uncertain. Eng. Syst. Part A Civ. Eng.* 2 (2016) B4016003. doi:10.1061/AJRUA6.0000872.
- [37]E.N. Chatzi, M.D. Spiridonakos, Incorporating Uncertainty in Vibration-Based Monitoring and Simulation, in: Fourth Int. Conf. Soft Comput. Technol. Civil, Struct. Environ. Eng. (CIVIL-SOFT-COMP 2015), Prague, Czech Republic, 2015.
- [38]R.P. Klis, E.N. Chatzi, M. Spiridonakos, Validation of Vibration Monitoring via Spectro-Temporal Compressive Sensing for Wireless Sensors Networks using bridge deployment data, in: Eighth Int. Conf. Bridge Maintenance Safety Manag. (IABMAS 2016), Foz do Iguaçu, Brazil, 2016.
- [39]J.S. Bendat, A.G. Piersol. *Random Data: Analysis and Measurement Procedures*. 4th ed. Hoboken, New Jersey: John Wiley & Sons, 2010.
- [40]A. Novakovic, J. Meyer, R. Bischoff, G. Feltrin, M. Motavalli, A. El-Hoiydi, A. Restrepo, J.-D. Decotignie, Low power wireless sensor network for monitoring civil infrastructure, Technical report, Empa, Swiss Federal Laboratories for Materials Testing and Research. CSEM, Swiss Center for Electronics and Microtechnology, 2009.